

A State-of-the-art Survey of U-Net in Microscopic Image Analysis: from Simple Usage to Structure Mortification

Jian Wu ^a · Wanli Liu ^a · Chen Li ^a, ✉ ·
Tao Jiang ^b · Islam Mohammad Shariful ^c ·
Hongzan Sun ^d · Xiaoqi Li ^a · Xintong Li ^a ·
Xinyu Huang ^e · Marcin Grzegorzek ^e

Abstract Image analysis technology is used to solve the inadvertences of artificial traditional methods in disease, wastewater treatment, environmental change monitoring analysis and convolutional neural networks (CNN) play an important role in microscopic image analysis. An important step in detection, tracking, monitoring, feature extraction, modeling and analysis is image segmentation, in which U-Net has increasingly applied in microscopic image segmentation. This paper comprehensively reviews the development history of U-Net, and analyzes various research results of various segmentation methods since the emergence of U-Net and conducts a comprehensive review of related papers. First, This paper has summarizes the improved methods of U-Net and then listed the existing significances of image segmentation techniques and their improvements that has introduced over the years. Finally, focusing on the different improvement strategies of U-Net in different papers, the related work of each application target is reviewed according to detailed technical categories to facilitate future research. Researchers can clearly see the dynamics of transmission of technological development and keep up with future trends in this interdisciplinary field.

Keywords Microscopic image analysis · U-Net · Image segmentation · Deep learning · Convolutional Neural Network

✉ Corresponding author
E-mail: lichen201096@hotmail.com

^a Microscopic Image and Medical Image Analysis Group, College of Medicine and Biological Information Engineering, Northeastern University, China

^b School of Control Engineering, Chengdu University of Information Technology, China

^c College of Software Engineering, Northeastern University, China

^d Shengjing Hospital of China Medical University, China

^e Institute for Medical Informatics, University of Luebeck, Germany

1 Introduction

1.1 Background Knowledge of Microscopic Images

Microscopic image refers to the image use to see in a microscope [1]. There are many types of microscopes: The general magnification of the optical microscope is generally 1500-2000 times [2–4], which has never exceeded 2000 times. However, the maximum magnification of the electron microscope exceeds three million times, such as transmission electron microscope (TEM) [5], scanning electron microscope [6]. Scanning tunneling microscope magnification up to 300 million times [7]. Furthermore, there are other types of microscopes, such as atomic force microscope [8], Raman microscope and cryo-electron microscopy [9, 10].

Microscopic image analysis has a wide range of application scenarios, such as microorganism image analysis [11–13], histopathological image analysis [14, 15], cytopathological image analysis [16, 17], metal structure analysis [18], rock structure analysis [19], soil structure analysis [20], material structure analysis and image analysis in plant pathology [21, 22].

1.2 Background Knowledge of Intelligent Microscopic Image Analysis

Manual operations of microscopic image analysis has some limitations, including:

- In the case of big data, it takes a long time.
- Operator has a heavy workload.
- Analysis of experimenters is easy to be subjective.
- Poor quantification.

Therefore, upcoming technologies should be introduced to this field to improve the level of image analysis.

As mentioned above, efficient artificial intelligence technology is introduced to the field of microscopic image analysis, which can effectively solve the above problems. First of all, computer efficiency is high and big data problems are easy to solve. Secondly, computer assistance can efficiently reduce the amount of hardwork. The third point, the computer is more objective. Finally, computer algorithms can quantitatively output the numerical results [23]. Especially, deep learning is the game changer and effective machine learning technology in the field of artificial intelligence in recent years, which has a high accuracy (ACC) rate. With the increasing amount of training data, the ACC rate is higher [24]. Deep learning [25] has a strong learning ability, wide coverage, adaptability and good portability. In different deep learning methods, CNN has the characteristics of non-contact and high precision for image recognition, classification and other operations. CNN is extremely applicable to this non-contact method in the process of image segmentation, detection, identification and classification, which can directly take image data as input [26].

Among all well-known CNN methods, U-Net [27] is clearly the most successful model for microscopic image segmentation, which does not require too many training data to obtain better segmentation results. Furthermore, the training and test time of U-Net is short, which supports a practical possibility for some real tasks, such as histopathology image analysis, microorganism image analysis and cell image analysis.

1.3 Typical U-Net Architecture

U-Net is originated from Fully Convolutional Networks (FCN), which is a semantic segmentation network [27, 28]. This network is named U-Net because of the U-shaped network structure, which is very suitable for medical image segmentation. The network structure is shown in Fig. 1. Structure of U-Net is symmetrical. The left side is the encoder which can extract the input features, the right side is the decoder, which can output the encoded features as a picture. Red square represents down-sampling, green square represents up-sampling and conv 1×1 represents the convolution operation with 1×1 as the core network. The networks on the left are the traditional convolutional layer and pooling layer. The 3×3 convolution and rectified linear unit (ReLU) activation function are performed twice and there is a 2×2 maximum pooling. The process is repeated four times and the filter is doubled at each stage. The right part uses the 2×2 transposed convolution to up-sampling. After performing the 3×3 convolution and ReLU activation function twice, it is also executed four times in a loop and the filter is reduced by half after each up-sampling. Finally, add a 1×1 convolution plus SIGMOID activation function to get the result. In addition, every time downsampling is performed when preparing for pooling, it will be fused to the feature map after transposed convolution, so that the output on the encoder can be directly connected to the decoder to continue propagation. It can be seen that the network is not fully connected. This is also an end-to-end image, that is, the input is an image and the output is also an image.

1.4 Motivation of This Survey Paper

Because of the efficiency and popularity of U-Net in microscopic image segmentation, many researchers choose to use it. Currently, there are some review articles involving U-Net, but there is no survey that focuses on U-Net in microscopic image analysis. Hence, we decide to prepare this survey paper to organize and summarize latest works for future work as a reference.

[29] introduces the development of segmentation neural network from the perspective of deep semantic segmentation of natural and medical images, including the development of U-Net and the variant of U-Net. There are 163 references in this paper, but only 16 are about microscopic image analysis. In the work of [30], a review of U-Net is given from the use of U-Net in different

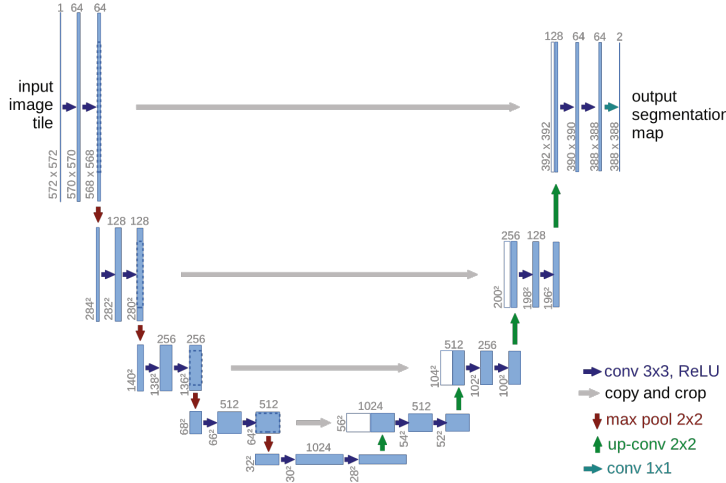


Fig. 1: The network structure of a typical U-Net [27].

application scenarios. There are 63 references in this work, but only eight references about microscopic image analysis are discussed. Compared with the above published reviews, we summarize 158 related works from 2015 to 2021, involving microorganism images, histopathological images, cytopathological images, rock microscopic images, metal microscopic images, plant microscopic images and material microscopic images. Our survey paper can provide services for the following two groups of people: (1) People who focus on microscopic image analysis; (2) People who do related to deep learning research and development, such as U-Net.

1.5 Structure of This Paper

The general structure of this paper is as follows: The first section summarizes the background of microscopic images, development status, motivation for this work and the structure of the paper. Section two describes the application scenarios of the unmodified U-Net. The third section writes the deformation method of U-Net under the primary changes and the dataset and application scenarios that it is good at segmenting after deformation. The fourth section is about some advanced and complex changes with Residuals in U-Net. This section contains many different types of changes.

2 Undeformed Classic U-Net

This section discusses about the unmodified U-Net in microscopic image segmentation and summarize the literature.

2.1 Applications in Cytology

In [27], U-Net is proposed to solve a problem of microscopic image segmentation. In this work, original images (512×512 pixels) are resized into 572×572 pixels to fit the input scale of U-Net. The method is applied to three datasets. Neuron structure has 30 pieces of training data. First, “PhC-U373” dataset has 35 training images with a small number of annotations. Second, “DIC-HeLa” dataset has 20 training images, some of them are annotated. At last, “PhC-U373” and “DIC-HeLa” obtain intersection over union (IOU) of 92.03% and 77.56%, respectively. Segmentation results are show in Fig. 2. In Sec. 3.1.1, we will discuss about 3D U-Net.

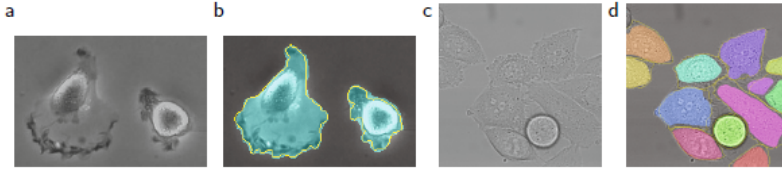


Fig. 2: Results of the method proposed in [27] Fig.4. (a) An original image in “PhC-U373” dataset. (b) Segmentation result of (a). (c) An original image in “DIC-HeLa” dataset. (d) segmentation result of (c).

In [31], undeformed U-Net can accurately segment corneal nerves. A dataset contains 30 people is tested, of which 10 are healthy and 20 are sick. This dataset is adjusted appropriately: first, outermost periphery (10 pixels) of the image to be analyzed is cropped. In addition each image is reduced to 0.7 times of the original size. Experimental result shows that SE reaches 97.2%.

In [32], an original U-Net is used to automatically segment nerve cells. In this paper, a classification task of excitatory, inhibitory neurons and glia cells is also performed. The original U-Net is trained on 126 images containing 5000 cells and an experimental result of an ACC of 93.2% is obtained.

Since the change of density of corneal endothelial cells (CEC) can monitor corneal diseases. In [33], a baseline U-Net is used to automatically segment corneal endothelium in a large set of “real-world” specular microscopy images. Compared with the baseline U-Net [27], neural network structure used for segmentation that has no structural changes. A mirror microscope database containing 16000 images (from corneal consultation service) is selected to evaluate this method and 158 training images are randomly selected as the training set. Finally, the experimental results with a CEC recall (RE) of 34% and an ACC of 84% are obtained.

2.2 Applications on Microorganisms

In [34], Tuberculosis (TB) cords are segmented by U-Net, taking into account the ACC of U-Net segmentation of TB cords. This method is also easy to operate when small reserve of expertise. Datasets are obtained through image reconstruction, a total number 300 images, of which 120 sub-images form the training set and 30 sub-images form the test set. Then, U-Net processes and segments sub-images. Finally, this method connects each sub-image to TB cords for the full images and the segmentation is completed. Finally, this work achieves an IoU of 88% and an ACC of 92.01%.

In [35], in order to reduce the time and physical waste of the operator, U-Net is used to segment the parasites in the blood to implement an automated system. This method is tested on a private dataset composed of 974 images. In the dataset, 600 images form the training set and 200 images form the testing set. The result shows that this method obtains an ACC of 63.04% and a Dice similarity coefficient (DICE) score of 68.25%.

2.3 Other Applications

In [36], in order to evaluate the geological characteristics of the rock samples, U-Net is used to segment the scanning electron microscope (SEM) images of it (as shown in Fig. 3). The dataset contains 8000 rock slice images, of which 80% are used for training and 20% for testing. The experiment result shows that the highest IOU reaches 93.2%. It can be seen that when processing texture features, U-Net has a good segmentation performance.

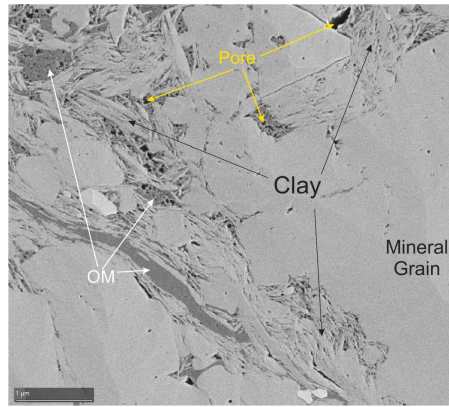


Fig. 3: An example of electron SEM image in [36] (Fig.1).

In [37], a new method of detecting nanoparticles is proposed, in which U-Net is used to segment nanostructures. The dataset has eight TEM images synthesized by Fe_3O_4 nano-particles and nine images of Fe_3O_4 nano-particles

smeared with silica, a total of 17 images. The experiment obtains an Acc higher than 90%.

In [38], because manual segmentation of nanostructured surface images is time-consuming and requires high professionalism. Therefore, it is necessary to develop an automated method for segmenting nanoparticles based on U-Net. A method based on U-Net is better than the traditional automation method. The experimental dataset contains 728 images of gold nanoparticles generated by the atomic force microscope (AFM) in the absence of moisture, of which 75% are used as the training set and 25% are used as the test set. When banding, the average rate of U-Net pixel change is 12.2%. The result of segmentation with U-Net is shown in Fig. 4.

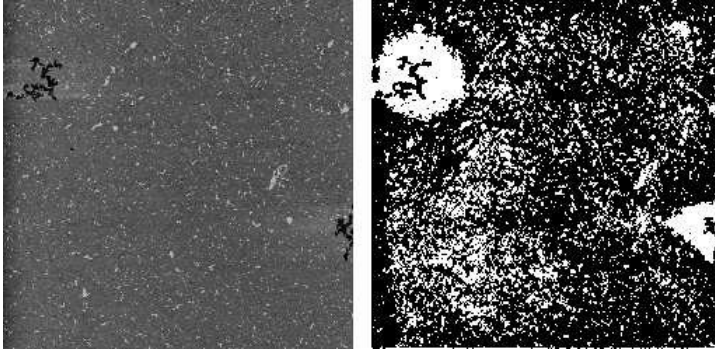


Fig. 4: An example of a multilayer image segmented using a U-Net model. This figure corresponds to Fig.9 in [38].

Skin healthy condition is evaluated through detection and analysis of blood vessel structure. In [39], a fully automatic method using a baseline U-Net is developed to segment the blood vessel structure in dermoscopy color images. This work utilizes a dataset from the University of Naples, Italy and the University of Graz, Austria, which contains 74 images of different types of blood vessel patterns in total. In the dataset, 80% of the samples are used for training and the remaining 20% are used for testing. The final experimental results are: a sensitivity (SE) of 85% and a specificity (SP) of 81%.

Many diseases can be diagnosed by retinal blood vessels, in [40], the original U-Net is used to segment Scanning Laser Ophthalmoscopy (SLO) (introduced by [41]) images. SLO assists blood vessels to be extracted features better. This proposed method is evaluated by IOSTAR [42]. In IOSTAR, 20 images form the training set and 10 images form the test set. The proposed method obtains an experimental result of an SE of 80.38%, a SP of 98.01%, an ACC of 96.95% and an area under curve (AUC) of 97.71%, respectively.

Since a method of manually obtaining tissue sections can easily introduce errors (such as deformation, tissue fracture). Therefore, the baseline U-Net [43] is developed to segment the undesired areas in whole slide images (WSIs) to

reduce errors. This proposed method can be used in the preprocessing step of WSIs automated analysis. The method may prevent the damaged area from being used. Meanwhile, the classification task is carried out by the baseline U-Net. Original WSIs are classified as Damaged and non-Damaged classes. This work utilizes a dataset from the archives of the Department of Pathology at the Military Institute of Medicine in Warsaw, Poland. The dataset contains 34 brain tissue cohorts corresponding to brain tumor areas (meningiomas and oligodendrogliomas) in total. However among the dataset, 10 WSIs for training and 24 WSIs be used in testing. Regarding Ki-67 brain tumor specimens segmentation, an experimental result is as follows: $SE = 0.83$, $SP = 0.92$, precision (PR) = 0.80, $ACC = 0.90$ and $IoU = 0.69$.

2.4 Summary

From the above analysis and review we can reach to a conclusion that the significant segmentation performance of U-Net on microscopic images, the original U-Net without any changes is often used to perform segmentation tasks and achieve good results. It shows that U-Net has strong versatility. U-Net also has wealthy application scenarios, such as cytology, histopathology, microorganism and nanoparticle image analysis. From birth of U-Net in 2015 to 2021, the original U-Net is used in a total number of papers that are listed above. With the development over the time, more and more variant network structures based on U-Net appears. In the subsequent analysis of the deformed structure section, the specific U-Net based on deformed network structure introduced. Tab. 1 is a summary of the evaluation indicators and results in the paper using the original U-Net.

3 Simple and Low-level Deformable U-Net

From the above section we can see: in most cases, the original U-Net segmentation without any changes performed well. However, firstly, U-Net published in 2015. In recent years, a large number of new network structure changes appear, such as: many new network modules are proposed and new ideas in skip connection are proposed. Secondly, U-Net can not fit all datasets perfectly. In many cases, the segmentation performance is not ideal, therefore, it is appropriate and simple to change the U-Net for better performance over the segmentation tasks. This section introduces some simple and conventional methods to change original implementation of U-Net structure.

Table 1: Summary of the original U-Net for segmentation tasks. The second column “Detail” shows the application object.

Aim	Detail	Year	Reference	Team	Data Information	CNN type	Evaluation
Segmentation	Glioblastoma-astrocytoma U373 cells	2015	[27]	O-Ronneberger	35 annotated images	U-Net	IoU = 92.03%
	corneal nerves	2018	[31]	A.Colonna	30 images 10 healthy images and 20 pathological images image is reduced to 0.7 times (256 X 256)	U-Net	SE = 97.2%
	nuclei	2019	[32]	S.Seong	126 images containing about 5000 cells	U-Net	ACC = 93.2%
	corneal endothelium	2019	[33]	M.C.Daniel	158 training images	U-Net	RE = 34%, PR = 84%
	TB cords	2020	[34]	L.Ballan	300 images 120 sub-images for training, 30 sub-images for test	U-Net	IoU = 88%, ACC = 92.01%
	the T. cruzi parasite	2020	[35]	A.Ojeda-Pat	974 images 600 images for training, 200 images for validation	U-Net	ACC = 63.04%, DICE = 68.25%
	rock slice SEM images	2020	[36]	Z.Chen	8000 images 6400 for train training, 1600 for validation	U-Net	IoU = 91.7%
	nano-particles	2019	[37]	A.B.Oktay	17 images	U-Net	SE = 78.59%, ACC = 96.59%
	nanostructured surfaces	2020	[38]	S.Farley	728 images 546 for training, 182 for test	U-Net	average proportion of pixels changed pixels changed = 12.2%
	blood vessel structure in dermoscopy color images	2018	[39]	J.Jaworek-Korjakowska	74 images %80 for training, %20 for test	U-Net	DICE = 0.84, SE = 0.85, SP = 0.81
	retinal blood vessels	2017	[40]	M.I.Meyer	30 SLO images 20 images 20 for training, 10 for test	U-Net	SE = 0.8038, SP = 0.9801 ACC = 96.95%, AUC = 0.9771
	empty areas in brain tissue WSIs	2018	[43]	Z.Swidarska-Chadał	34 WSIs Ki-67 staining 10 for training, 24 for test	U-Net	SE = 0.83, SP = 0.92, PR = 0.80 ACC = 90%, IoU = 0.69

3.1 Redesigned Convolution

3.1.1 3D Convolution

In [44], a 3D U-Net that replaces 2D convolution with 3D convolution is creatively proposed to achieve accurate semi-automatic segmentation of 3D datasets. Compared with baseline U-Net, 3D U-Net replaces all 2D operations in the paper [27] with 3D operations and adds Batch Normalization (BN) before each ReLU (similar addition BN’s approach is also reflected in the paper [45]). A dataset with 77 manually annotated *Xenopus* kidney slices under confocal microscopic is used in the experiment. Under the dataset, the proposed 3D U-Net obtains an IoU of 0.863 in the semi-automated test experiments of three-fold cross validation.

In [46], a 3D U-Net composed of 3D convolution combined with spatially constrained cycle-consistent adversarial networks is proposed. It solves the problem of high learning rate for manually labeling 3D datasets. The structure of this 3D U-Net is shown in Fig. 5. First, a subvolume of the original image volumes train spatially constrained CycleGAN (SpCycleGAN). Then, the above operations generate 3D synthetic data to evaluate the 3D U-Net. Finally, the proposed method obtains an ACC of 95.56%.

In [47], a 3D U-Net combined with a seeded watershed approach (SWS) is proposed. It solves a problem of the large amount of data in the 3D mi-

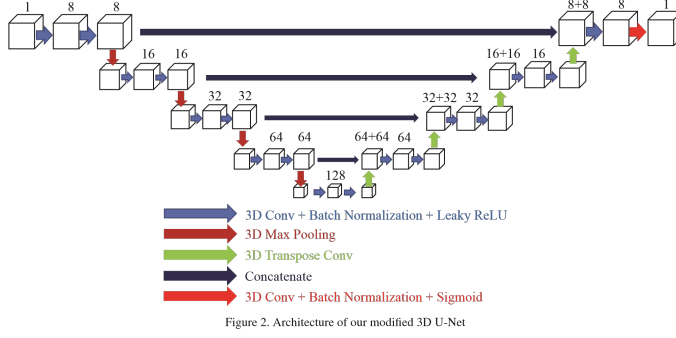


Fig. 5: The network architecture of 3D U-Net (corresponding to Fig.2 in [46]).

croscopic image of the cell membrane, which is not easy to segment. This method is tested on a training set (the training set comes from [48]) composed of 109296 *Arabidopsis thaliana* cells and a validation set composed of 972 single cells, which manually annotate 3D images. At the same time, 3D U-Net + watershed algorithm (WS), 3D U-Net + supervoxel merging approach (SV), multi-angle image acquisition, three-dimensional reconstruction and cell segmentation (MARS) [49], automated cell morphology extractor for comprehensive reconstruction of cell membranes (ACME) [50] are also tested by the dataset. The experimental results show that among these methods, U-Net + SWS performs best and it obtains a JI of 0.870 and a DICE of 0.931. Fig. 6 is the segmentation result of the method mentioned in [47].

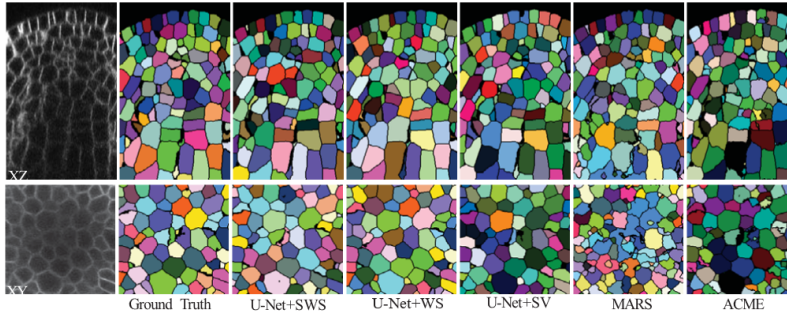


Fig. 6: A comparison of the image segmentation results of the proposed method in [47] (Fig.3), where the top row shows XZ-plane and the bottom row shows XY-plane.

In [51], a 3D U-Net is proposed to fit the non-isotropic nature of serial section Transmission Electron Microscopy (ssTEM) data, the sparsity of synapses improves the performance of segmentation and detection of insect nervous system. Challenge on Circuit Reconstruction from Electron Microscopy Images

(CREMI) datasets from Medical Image Computing and Computer Assisted Intervention Society (MICCAI) is used in the experiment. It contains 6 volumes of nerve tissue under an electron microscope, of which 75% are used in the training set and 25% are used in the validation set. The proposed 3D U-Net obtains the experimental results of CREMI score with an average of 50%.

In [52], because of the complex structure of neurons and poor imaging quality in some cases, a teacher-student learning framework based on 3D U-Net [44] is proposed to segment neurons to obtain higher ACC and efficiency. Like [44, 46, 47, 51], the teacher-student learning framework uses 3D convolution as the basic unit. Unlike [44, 46, 47, 51], first, the teacher-student network is divided into 2 parts: Teacher network and student network. Second, Residual modules (the specific usage of Residual modules is detailed in Sec. 4) are added to the teacher-student network. A data is obtained from the Janelia dataset from the BigNeuron project (contains 42 images of adult *Drosophila* nervous system, 38 images for training and 4 images for testing). A PR-RE curves in [52] shows that the teacher-student network can obtain more accurate segmentation performance.

3.1.2 Other Convolution

In [53], deformable U-Net with variable convolution is used to segment and classify sickle cell disease (SCD) cells. Similarly, [54] is the study of SCD cell segmentation from the same team. Compared with U-Net, in addition to variable convolution, deformable U-Net has only three deformable convolution blocks in the encoding and decoding parts respectively. A dataset with 128 SCD cells obtained from University of Pittsburgh Medical Center (UPMC) is used in the experiment. The deformable U-Net is tested under the dataset. It obtains a segmentation ACC of 97.8% and a classification ACC of 82.7%. The segmentation results of proposed method in Fig. 7.

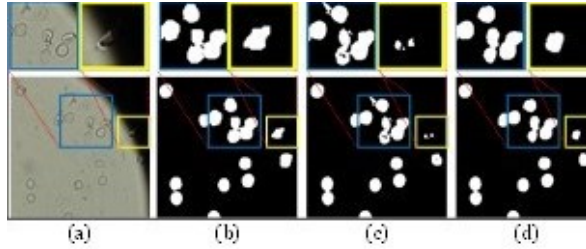


Fig. 7: The cell segmentation results in [53] (Fig.3). (a) Raw images; (b) Ground truth images; (c) Segmentation result of U-Net; (d) segmentation result of deformable U-Net.

In [54], in order to solve the inaccurate segmentation and classification of SCD cells are caused by the change of cell shape and the image blur caused by

noise and artifacts, deformable U-Net with variability convolution is proposed. The structure of the deformable U-Net is shown in Fig. 8, which is consistent with the network structure of [53]. The ordinary convolution becomes the deformable convolution and the convolution block is reduced. In contrast to [53], the dataset in this paper is a public dataset of red blood cells (RBCs) of SCD patients, from [55], there are four different types of 266 original images. Under the dataset, they proposed new network is tested to achieve a segmentation ACC of 99.12% and an IoU of 44.15%.

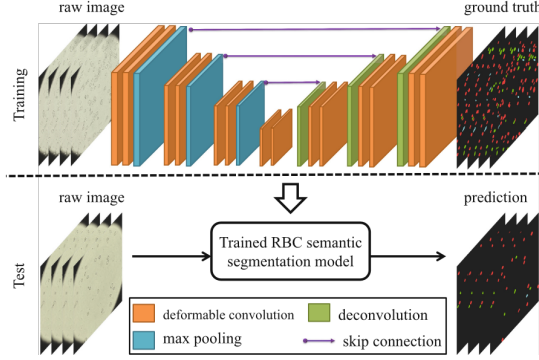


Fig. 8: The network architecture of the deformable U-Net in [54] (Fig.2).

In [56], a Match Feature U-Net used in the field of medical image dynamic reception is proposed to perform cell segmentation. Like [44, 46, 51–54], Match Feature U-Net improves the ability to segment-specific or public datasets by changing basic convolution units. Unlike the above works that plain convolution becomes 3D convolution and deformable convolution, an adaptive receptive field mechanism is embedded in the Match Feature U-Net. The mechanism is introduced by adding a large number of Dynamic Convolution Units with Adaptive Receptive Field (ARF) convolution. Match Feature U-Net is evaluated by 670 cell nuclei (each original image is augmented to 16 times) from Data Science Bowl 2018, of which 80% is used for 5-fold cross-validation and 20% is used for testing. Finally, the Match Feature U-Net with Match operator obtains a MIoU of 91.83% experimental results. Similar technical methods are not only used for cell segmentation. In [57], the U-Net-based method of changing convolution is applied to cell counting and centroid localization.

In [58], a variant U-Net composed of Inception modules (introduced in [59]) with dilated convolution is proposed. The variant U-Net is proposed to obtain accurate segmentation of trophoctoderm (TE) and to achieve an automatic evaluation of the quality of human embryos. It is different from deformed U-Nets formed by Inception modules, dilated convolutions with different dilation rates in the variant U-Net replaces plain convolutions. Datasets come from [60] (contains 235 human blastocyst images) and a private dataset (including 592

human blastocyst images), of which 70% are used as the train set and 30% are used as the test set.

3.2 Add convolution block, reduce convolution block

In [61], a deformed U-Net is used to segment images with minimal annotation. In addition to the reduction in the number of feature maps of the convolutional layer in the encoding and decoding part, the other parts of the deformed U-Net are consistent with the classical U-Net. One of the advantages of the deformed U-Net: the training parameters of the structure are reduced, which prevents overfitting. The deformed U-Net is tested by the Rift Valley virus dataset (there are 143 TEM images) [62] and obtains a DICE of 0.900 and an IoU of 0.831.

In [63], in order to identify whether cells are normal or circulating tumor cells (CTCs), a modified U-Net is used to automatically segment the cells. The modified U-Net has three more layers in the encoding and decoding parts than the original U-Net structure. In addition, an additional 3×3 convolution and ReLU are added to each layer in the decoding part. Like [64, 65], the modified U-Net from [63] has a change in the number of convolutional layers compared with the baseline U-Net. Unlike [64, 65], the modified U-Net from [63] segmentation of cell images in the blood instead of histopathological images. In terms of data, tumor cell datasets from the Oncology Institute of Cluj-Napoca are used. 120 image data expand into 56000 images by generating small patches, furthermore, 70% of it is used as the training set and the rest is the test set. The final result shows that under their dataset, an ACC of 99.81% is obtained.

By observing corneal endothelial cells, information about corneal health can be obtained in time. Because of the size of endothelial cells in the specular microscope image needs to be analyzed, a U-Net-based CNN is developed to segment endothelial cells [66]. Improvements compared with the baseline U-Net are described as follows: First, convolution blocks are reduced and the downsampling is reduced twice (the same operation is in [53]). Second, the number of feature vectors in each layer is 50% from the original. A dataset employed in the experiment contains 30 images of the corneal endothelium. In the dataset, 50% of the samples are used for training and the remaining 50% are used for testing. A result of the experiment is that a DICE reaches 86%.

In [64], a new variant U-Net (named US-Net) is proposed for robust nuclei instance segmentation in histopathology images. Like [65], US-Net has a post-processing part after the output layer. Unlike [65], US-Net combines a single shot multibox detector (SSD) to form a post-processing sub networks, rather than simply adding a post-processing layer. A training dataset curated by the Segmentation of Nuclei in Images Contest (SNIC) and the Medical Image Computing and MICCAI. 32 patches from SNIC and 30 patches from MoNuSeg are pre-processed to obtain 878 patches, of which 650 patches are used for training and 228 patches are used for evaluation. an experimental

result shows that the proposed US-Net performs better than many advanced nuclear detection and segmentation networks.

In [65], noise-tolerant U-Net is proposed to fully automate the segmentation of histopathological images. Two differences between the noise-tolerant U-Net and the baseline U-Net are: noise-tolerant has two less convolutional blocks. However, it adds a noise-tolerant layer after a softmax output layer. Like [63, 64], noise-tolerant U-Net changes the number of layers of convolution. Unlike [63, 64], noise-tolerant U-Net reduces the convolutional layer. A dataset includes five groups of histopathological images of Duchenne Muscular Dystrophy (DMD). The first group contains 110 images as a training set and the remaining four groups (100 images in each group) are used for validation and comparison.

However the original network requires more annotated images. Throughout the study of [67], a modified U-Net that only needs a small amount of annotated images and has a more appropriate amount of calculation is proposed. Compared with the classical U-Net, this modified U-Net has three main improvements: reducing the number of filters, adding a BN layer after the convolutional layer and adding rectified-Adaptive Moment Estimation (Adam). From ISBI cell tracking Challenge, 120 images (data augmentation from 30 images to 120 images by cutting and flipping) of the *Drosophila* first instar larva ventral nerve cord (VNC) are used to evaluate the modified U-Net. Experimental results show that an IoU of 92.54% is obtained.

3.3 Composite Structure Appearance Multiple U-Net Chains

In [68], since the mitochondria and synapses in the mouse brain under the electron microscope are not easily segmented, a two-stream U-Net with two coupled U-Nets is proposed. Two-stream U-Net is different from the classic U-Net [27]. First of all, it consists of two symmetrically distributed U-Nets. Furthermore, one U-Net acts on the source domain and the another one acts on the target. Finally, the weight is shared by two U-Nets. Like [69, 70], two-stream U-Net consists of two similar U-Nets. Unlike [69, 70], two U-Nets of two-stream U-Net are trained by the source domain and the target domain, respectively. However, in [69] and [70], the input of U-Net at the back is related to the output of U-Net at the front. TEM volumes of mouse somatosensory cortex and cerebellum are used to test the two-stream U-Net and a JI of 0.7230 is obtained. The architecture of two-stream U-Net is shown in Fig. 9.

In many segmentation tasks, the traditional encoder, decoder and skip connection structure cannot complete the task perfectly and there are few channels for information flow to circulate. In [70], LadderNet is proposed to solve the problem. The same point as [68, 69], the weights are shared between the two U-Nets. The difference from [68, 69], LadderNet shares the weights in the decoding part of the first U-Net and the encoding part of the second U-Net. But, two-stream U-Net shares weights in the decoding part of the two U-Nets. A dataset is obtained from one source: the CHASE DB1 dataset (contains 28

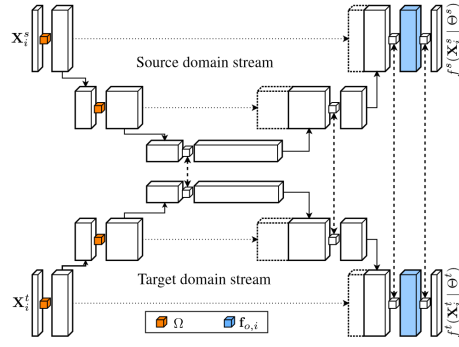


Fig. 9: The network structure of two-stream U-Net in [68] (Fig.2).

retinal images, of which 70% is used for training and 30% is used for testing). In the dataset, 0.8031 F1-score, 0.7978 SE, 0.9818 SP, 0.9656 ACC and 0.9839 AUC are obtained.

In [69], a stacked double U-Net is proposed to obtain better segmentation ACC and is named DoubleU-Net. Like [68, 70], encoding and decoding ideas of U-Net are not changed. Unlike [68, 70], first, the encoding part of a U-Net in DoubleU-Net is replaced with VGG-19 [71]. Second, the information flows from the previous U-Net encoding part to the next decoding part. Third, DoubleU-Net is evaluated by the alike-microscopic dataset. DoubleU-Net is tested on the CVC-ClinicDB dataset [72] to obtain a DICE of 0.9239, a mean Intersection over Union (mIoU) of 0.8611, a 0.8457 RE and a 0.9592 PR. The segmentation results of DoubleU-Net are shown in Fig. 10.

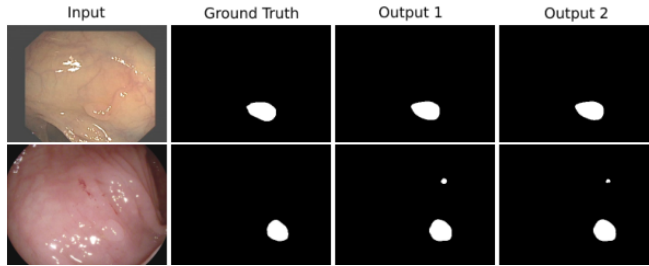


Fig. 10: The segmentation results of DoubleU-Net in [69] (Fig.3).

The variant structure based on U-Net is not easy to segment adjacent cells, in [73] DeepSplit is proposed to segment the cell contact areas. Like [68–70], DeepSplit has multiple U-Net chains with a composite structure appearance. Unlike [68–70], DeepSplit only has one encoder branch and two decoder branches. The second decoder branch is a separate branch, its main purpose is to segment the cell contact areas. This method is evaluated on an MCF-10a epithelial breast cells dataset (contains 50 manually annotated images, of

which 80% is used for training, of which 10% is used for verification and of which 10% is used for testing). Finally, a cell detection score (CDS) of 0.903 is obtained.

In [74], a MUnet nested with three U-Nets is proposed, which is used to segment the image of morphological patterns of human skin under reflectance confocal microscopy (RCM). Because the traditional method is time-consuming, MUnet is used to assist in the diagnosis of this type of skin cancer. 56 RCM mosaics (46 mosaics are used for training and 10 mosaics are used for testing) annotated by experts with 6 types of labels are used to evaluate MUnet. Because three nested U-Net structures are designed, the segmentation operation of MUnet can be performed at different resolutions. Finally, for the background segmentation under the dataset, MUnet obtains a 72.89% SE, a 95.26% SP, a 78.36% DICE and a 84.71% PR.

In [75], a Triple U-Net is proposed for nuclear segmentation to avoid blurry tumor nucleus boundaries and overlapping tumor cells as much as possible. Like [74], the Triple U-Net is composed of three U-Net branches: a red-green-blue (RGB) branch, a Hematoxylin branch and a Segmentation branch. Unlike [74], two branches of the Triple U-Net are composed of Progressive Dense Feature Aggregation Module (PDFA) based on the densely connected block (be introduced by [76]). This work utilizes the MoNuSeg dataset from 7 organs which contain 30 images in total, 21000 nuclear boundaries are annotated. In the total dataset, 16 images are used for training and 14 images are used for testing. Comparison of Triple U-Net and existing nuclei segmentation models, the final Triple U-Net result is the best (0.837 DICE).

3.4 Attention U-Net

An attention mechanism is introduced into U-Net in [77] and applied to a CT dataset to highlight features. In [78], an ATTention U-Net (ATT-UNet) is proposed to segment an iris to solve a problem that a segmentation network is susceptible to irrelevant noise pixels outside the iris area. ATT-UNet enables a network to focus on a region of interest (ROI), avoid wasting time and over-computing features of irrelevant regions. The purpose of the attention mechanism is introduced to guide ATT-UNet to learn more features to separate the iris and non-iris pixels. An attention mask is generated to evaluate the most likely areas of the iris and a bounding box regression module is used to evaluate the coordinates. Furthermore, the attention mask guides ATT-UNet to segment the specific area. A dataset employed in the experiments comes from UBIRIS.v2 [79], of which 500 images are used as the training set and 500 images are used as the test set. In the end, an experiment result shows: an IoU of 91.37% is obtained.

In [80], an attention guided U-Net with atrous convolution (AA-UNet) is proposed to segment retinal blood vessels. A precise segmentation of retinal blood vessels has an important auxiliary role in the diagnosis of diabetes, hypertension and other diseases. Like [78], an attention module is used to

force the network to pay attention to ROI. Unlike [78], atrous convolution replaces ordinary convolution in the feature blocks, which is beneficial to increase the receptive field. AA-UNet is tested on three retinal vessels segmentation datasets (DRIVE [81], STARE [82] and CHASE_DB1 [83]). The DRIVE (Digital Retinal Images for Vessel Extraction) dataset contains 40 fundus images, of which 20 images are used for training and 20 images are used for testing. Under the DRIVE dataset, AA-UNet obtains 95.58% ACC, 82.16% F1-scores, 95.68% Jaccard similarity (JS) and 98.47% AUC.

In [84], in order to segment curved structures (such as blood vessels), CS-Net is proposed to assist experts in diagnosing diseases. Channel attention block (CAB) and spatial attention block (SAB) with attention ideas are integrated into the baseline U-Net. Attention idea appears in the form of a module after the encoder. STARE is a fundus dataset used to evaluate this proposed method. An experimental result is obtained by CS-Net (97.52% ACC, 0.88.16% SE, 98.40% SP and 99.32% AUC).

In [85], a connection sensitive attention U-Net (CSAU) is proposed to segment retinal blood vessels. Like [80, 84, 86], CSAU is proposed to segment retinal blood vessels. Unlike [80, 84, 86], a connection sensitive loss is proposed and combines with attention gates. CSAU is trained on the DRIVE, STARE and HRF datasets, respectively. STARE contains 20 fundus images, of which 50% are used for training and 50% are used for testing. Under the test data of STARE, an experimental result of CSAU is as follows: an F1-score of 0.8435, a SE of 0.8465 and an ACC of 0.9673.

In [86], a novel multi-path recurrent U-Net with attention gate (MPAR) is developed to segment retinal fundus images. An innovative idea of many variants of U-Net is that attention is integrated into the baseline U-Net [78, 80, 84, 85, 87, 88]). However, in MPAR, Attention Recurrent Unit (formed by combining recurrent neural network and attention) can further improve target features. Two datasets (Drishti-GS1 dataset [89] and DRIVE dataset [81]) are used to evaluate MPAR. The Drishti-GS1 dataset has 101 retinal fundus vascular images. For the Drishti-GS1 dataset, in the training phase, 50 images are used as the training set. In the testing phase, 51 images are used as the test set. Experimental results of testing MPAR under the DRISHTI-GS1 dataset are as follows. For optic disc segmentation, an ACC of 99.67% and a DICE of 98.17% are obtained. For optic cup segmentation, an ACC of 99.5% and a DICE of 89.21% are obtained.

In [87], a method based on ATT-UNet and graph-based Random Walk (RW) is proposed to extract nucleus and cytoplasm from overlapping cervical cells. This method proposed is mainly the following four steps: (1) ATT-UNet is used to separate the nuclei; (2) images are acquired by polar coordinate sampling; (3) ATT-UNet predicts the cytoplasm boundary; (4) RW is used to refine the cytoplasm boundary. Because of the repeated operation of the encoding part, some spatial detail information is lost. Attention Gates (AG) [77] is used to obtain the missing information. The architecture of Attention Gate mentioned in Fig. 11. The experimental data are training images of the ISBI 2014 Challenge Dataset. 135 synthetic cervical cytology images from eight

training depth of field (EDF) images are splited into 45 images (train set) and 90 images (test set). Under the test set, a 0.93 DICE is obtained.

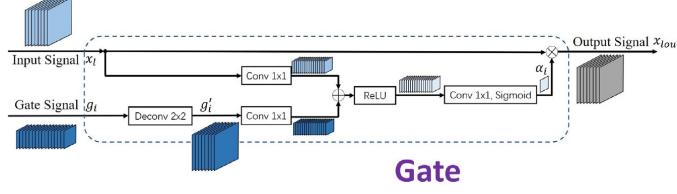


Fig. 11: The network architecture of Attention Gate in [87] (Fig. 3).

In [88], irregular cell boundaries are often difficult to segment. Residual Attention U-Net (ResAttU-Net) is proposed to segment the cells in fluorescence widefield microscopy images. Like [87], AG is applied to ResAttU-Net. Unlike [87], Residual blocks [90] are integrated into ResAttU-Net. This work utilizes a baby hamster kidney (BHK) cell dataset from Columbia University in the Department of Biomedical Engineering. After data enhancement such as random horizontal and vertical flipping, 4600 cell images constitute the training set, 1000 images constitute the training set and 500 images constitute the test set. This proposed method obtains good experimental results (SE=0.97, SP=0.93, F1-score=0.95, JS=0.91 and DICE=0.95).

In [91], in order to assist ophthalmologists in the diagnosis of eye diseases, a method that relies on data enhancement and combined with U-Net is proposed to segment retinal blood vessel images. Like [66], an identical structural deformation is applied to the baseline U-Net. Unlike [66], this method is to segment the retinal blood vessels images. 20 DRIVE training images generate 19,000 patches to form a dataset. From the training set, 90% of samples are used for training and the remaining 10% are used for validation. This experiment obtains satisfactory results.

In [92], in order to fully consider contextual information, a context-aware U-Net is proposed to conduct the segmentation tasks of the Drosophila first instar larva VNC. Like [93], the context-aware U-Net improves the long connection by placing a model on the connection. Unlike [93], the context-aware U-Net places a context transfer module instead of a Residual module. A dataset used for the Drosophila first instar larva ventral nerve cord images segmentation in experiments from [EM segmentation challenge \(ISBI 2012\)](#). A training data is 30 serial section transmission electron microscopy images. The context-aware U-Net obtains a segmentation result: A warping error of 0.000121, a rand error of 0.0212 and a pixel error of 0.0346.

3.5 Dense U-Net

A densely connected convolutional network (DenseNet) is proposed [?]. The feature of a dense U-Net is that in the dense block, each layer is directly connected to the previous layer. The structure of the dense block is shown in Fig. 12. The advantage of this structure is that the vanishing gradient problem can be alleviated. In [94], DenseNet is modified and integrated into U-Net to propose a new neural network and used to segment some trial scenes.

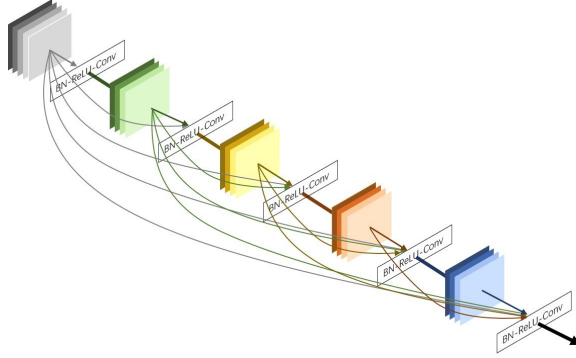


Fig. 12: The network architecture of dense block in [95] (Fig.6).

In [95], a new dense block-based U-Net is proposed to perform segmentation tasks of blood vessels. The structure of the new block-based dense U-Net is shown in Fig. 13. It differs from the baseline U-Net in: (1) dense block replaces ordinary convolutional blocks (in [75], a PDFA module improves densely connected block); (2) Parametric Rectified Linear Unit (PReLU) [96] replaces ReLU; (3) encoder and decoder part is missing a convolution block. two datasets (CHASE_DB1 dataset [97] and DRIVE dataset [81]) are used to evaluate the new dense block-based U-Net. The DRIVE dataset has 40 retinal fundus vascular images. For the DRIVE dataset from a diabetic fundus lesion screening organization, in the training phase, 20 images are used as the training set. In the testing phase, 20 images are used as the test set. Experimental results of testing the new block-based dense U-Net under the DRIVE dataset are as follows: 0.9834 SP, 0.7672 SE, 0.9559 ACC and 0.9793 AUC.

In [98], an improved U-Net combining patch-based learning strategy and dense idea is proposed to segment retinal vessels. Like [95], compared with the baseline U-Net, dense block replaces ordinary convolutional blocks and the number of convolutional blocks is reduced. Unlike [95], the Residual idea is applied before the dense block and the convolution block is reduced by two blocks in the encoder and decoder parts. This work utilizes two public datasets (DRIVE and STARE). For the DRIVE dataset, during the training process, 40000 image patches are extracted from 20 source images, of which

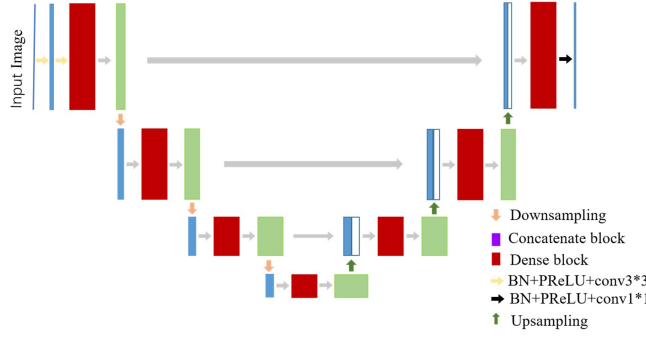


Fig. 13: The network architecture of dense U-Net in [95] (Fig.7).

10% are used for cross-validation. Finally, 0.7986 SE, 0.9736 SP, 0.9511 ACC and 0.9740 AUC are obtained.

In order to use deep learning models to assist pathologists in achieving precise treatment, in [99], a new improved U-Net (HistNet) is proposed for segmentation of colorectal histopathology. Like [95, 98], dense blocks are applied to U-Net. Unlike [95, 98], dense blocks are improved (modified dense block uses dilated convolution). To evaluate the proposed model thoroughly, the DigestPath 2019 dataset [100] and the Gland Segmentation (GlaS) dataset (in Histology Image Challenge held at MICCAI 2015) [101] are applied. For DigestPath 2019 dataset, it contains 660 tissue images from 324 WSI, the tissue images are randomly divided into training, validation and test sets at a ratio of 70 : 15 : 15. Finally, 92.36% DICE and 86.65% IoU are obtained by HistNet.

Since, biomedical image segmentation plays an important role in diagnosing diseases, therefore, a novel Multi-scale Dense U-Net (MDU-Net) is proposed to segment biomedical images [102]. Like [95, 98], MDU-Net uses a dense idea. Unlike [95, 98], MDU-Net is a multi-scale densely idea, more precisely, Cross Dense connections, Up Dense connections, Down Dense connections are widely used in the MDU-Net, but MDU-Net does not have dense blocks. A dataset containing 165 biomedical images (originate from Histology Image Challenge held at MICCAI 2015) is used. The dataset is divided into two subsets, the first subset (containing 85 images) is used for training and the second subset (containing 85 images) is used for testing. Finally, experiment reveals that a DICE obtained by this proposed method is 4.1% higher than baseline U-Net.

In [103], a Densely Connected Stacked U-Network (DCSU) is used to segment confocal microscopy images of filament. Unlike [95, 98, 102], DCSU is a cascaded U-Net (combination of multiple U-Nets, the output of previous level U-Net is related to the input of the next U-Net [104]) and dense connections occur between convolutional blocks of different U-Nets. A microtubule dataset containing 5032407 training patches is proposed to evaluate DCSU. Under the microtubule dataset, this proposed method obtains an IoU of 0.9439 and a Skeletonized IoU (SKIoU) of 0.9775.

3.6 U-Net redesigned Skip Connections

In [105], a simple and effective modified U-Net that redesigns the original U-Net skip connection is creatively proposed. It reduces the loss of information in the copy aggregation from the encoder to the decoder. For different datasets, the importance of each convolutional layer is different. The information carried by the third layer may be effective for the segmentation of the dataset or it may be the second layer. The advantage of this modified U-Net is that all copy aggregation operations contain all the depth feature information of the previous convolutional layer. A data from [Data Science Bowl 2018](#) containing 670 nuclear images are used. Under the dataset, an IoU of 92.63% core segmentation result is obtained. Fig. 14 shows the proposed deformable U-Net and the analysis of the variant thinking.

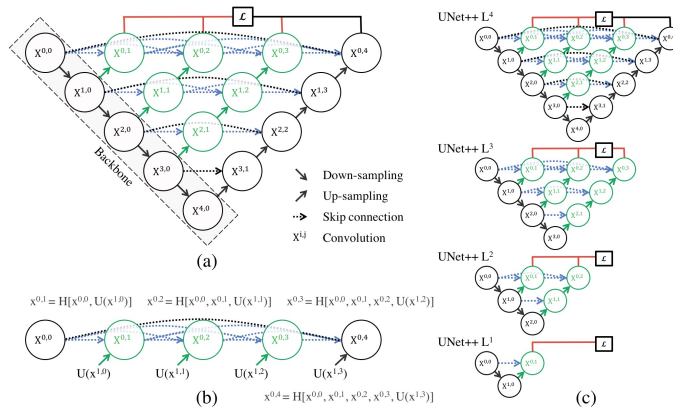


Fig. 14: The network structure of the deformable U-Net in [105] (Fig.1).

In [106], a U-Net that changes skip connection is explored in more depth (similarly, [105] is the study of skip connection from the same team). A purpose of the U-Net that changes the skip connection is to reduce the loss of information when convolutional layers of different depths are aggregated and connected. Like [105], the deformed U-Net is deleted some mandatory aggregations (or different depth features are extracted), different performances are obtained. Unlike [105], the deformed U-Net is evaluated by more datasets.

In [107], a powerful improvement U-Net++ is proposed to segment tiny breast cancer nuclei. The difference between the improved U-Net++ and the baseline U-Net++ [105] is that an Inception-Resnet-V2 network is integrated into U-Net++ and the network improves U-Net++ segmentation capabilities. This work utilizes a dataset from [108], which contains 141 RGB H&E stained estrogen receptor positive (ER+) breast cancer images in total. Finally, the dataset has a total of 3366 sub-images after being resized and cropped. The proportions of the training set, validation set and test set are 80%, 10% and

10%, respectively. The improved U-Net++ is evaluated by this dataset and obtains 0.9505 ACC, 0.5581 PR, 0.6035 RE and 0.5207 DICE.

Doppler optical coherence tomography (OCT) vessels images can observe the vascular structure and blood flow to facilitate surgery. So in [104], a cascaded U-Net (CU-net) is proposed to segment the vascular intensity images, the boundary image of the outer vessel wall and the inner blood flow lumen (this cascaded U-Net idea is also reflected in [103]). In Cu-Net, the first U-Net segment the intensity image, then the segmentation result is used as the input of the second U-Net (as a mask, it is better to select the region of interest and remove the non-target region). The above operations can reduce training time. This method is examined on a traceable dataset of Doppler OCT images of mouse arteries. The dataset used in the experiments is consists of 190 images, of which 150 images are used for training and 40 images are used for testing. These experimental results show that for the segmentation of the outer vessel wall boundary, CU-net obtains an ACC of $96.7\% \pm 0.2\%$, furthermore, for the segmentation of the contour of the inner blood flowing lumen area, CU-net obtains an ACC of $94.8\% \pm 0.2\%$.

In [109], a dyed particle usually needs to be divided manually by an expert and the reproducibility of the operation is low. Therefore, a simple and effective deformed U-Net is proposed to solve the problem and achieve precise segmentation. A dataset is composed of art papers printed by mixing carbon black pigments and inks, with a total of 60 images. First, improved U-Net #1 is obtained by changing the number of channels. Then, improved U-Net #1 outputs high-precision large particle segmentation results. Finally, the segmentation results are applied to improved U-Net #2 (delete some skip connections) to obtain the best segmentation results. Two different variants of U-Net combined with the proposed method flow obtain a root mean squares error (RMSE) of 45.2187 and a standard deviation of 7.8371.

Hence, the segmentation of retinal arterioles and venules has an important auxiliary role in the diagnosis of eye diseases. Therefore, in [110], an improved U-Net is proposed to segment arterioles and venules. Like improved U-Net #2 from [109] and improved U-Net from [110] deletes the connections. On the contrary, improved U-Net #2 from [109] and improved U-Net from [110] only deletes the fourth connection between the encoder 512-channel feature map. The segmentation results of the proposed method are shown in Fig. 15. This experiment uses a DRIVE dataset curated by a diabetic retinopathy screening program. DRIVE (contains 40 color fundus photographs) is used to evaluate six different segmentation methods. Finally, the improved U-Net obtains an optimal experimental result (0.870 SE and 0.980 SP).

In [111], in order to better realize target spore identification and spore count, an effective variant U-Net is proposed to segment wheat powdery mildew spore images. The variant U-Net has two differences from the baseline U-Net as follows: The variant U-Net deletes the three skip connections in the baseline U-Net and adds the pyramid pool module after the encoding is completed. Like improved U-Net #2 from [109] and improved U-Net from [110], the variant U-Net deletes some connections. Unlike improved U-Net #2 from [109]

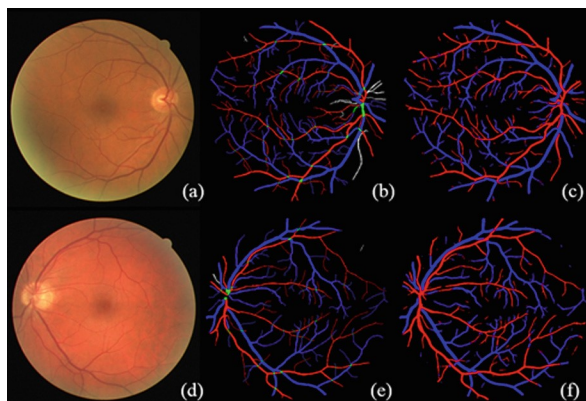


Fig. 15: Segmentation result in [110] (Fig.3). (a) and (d) are the original images; (b) and (e) are the ground truth images; (c) and (f) are the segmentation results.

and improved U-Net from [110], the variant U-Net from [111] only 1 connection between encoder 512-channel feature map is reserved. 835 wheat powdery mildew spore images are divided into a training set and a test set, of which 550 images are used as training set and 285 images are used as the test set. The variant U-Net obtains an MIoU of 91.48% experimental results.

3.7 Summary

From the survey above, since 2016, U-Net has improved, but after 2018, deep neural networks based on U-Net become more and more widely used in the field of biomedical image segmentation. The main reasons for this development trend are as follows: (a) More advanced computers are developed, which can handle more complex networks. (b) The improved U-Net architecture that can avoid problems such as over-fitting and enhanced computing time. Table 2 summarizes the work done by different teams in using the improved U-Net to analyze microscopic images.

Table 2: Summary of the improved U-Net for segmentation tasks. The second column “Detail” shows the application object.

Aim	Detail	Year	Reference	Year	Data Information	CNN type/points of improvement	Evaluation
semi-automatic segmentation	Xenopus tadpole zebra	2016	[54]		77 images	3D U-Net	IoU = 86.3%
segmentation	3D synthetic data	2018	[6]		3D synthetic data	3D U-Net	ACC = 95.56%
segmentation	cell membrane	2019	[17]		10226 cells for training, 972 cells for validation	3D U-Net combined with SWS	F1 = 87%, DICE = 93.1%
segmentation	nerve tissue	2018	[51]		6 volumes: 71% for training, 29% for validation	3D U-Net	CREMI score = 50
segmentation	neurone	2019	[53]		42 images		
segmentation	nerve	2019	[53]		38 images for training, 4 images for test	Teacher-student network: based on 3D U-Net	\
segmentation and classification	SCD cells	2017	[53]		129 images	variable convolution is applied	segmentation ACC = 97.8%, classification ACC = 82.1%
		2018	[53]		268 original images		segmentation ACC = 99.12%, IoU = 84.13%
segmentation	cell nuclei	2020	[54]		670 images: 80% for validation, 20% for test	Match Feature U-Net	IoU = 91.83%
segmentation	trophoblastum	2020	[54] 58		827 images: 70% for training, 5% for test	dilated convolution; Inception modules	\
segmentation	Rib V alloy virus	2018	[51]		140 TEM images	reduction in the number of feature maps of the convolutional layer	DICE = 90%, IoU = 83.1%
segmentation	circulating tumor cells	2018	[51]		5000 images: 70% for training, 5% for test	Correlation block increased	ACC = 99.81%
segmentation	endothelial cells	2018	[51]		30 images: 50% for training, 50% for test	Convolution blocks are reduced	DICE = 86%
segmentation	nuclei	2019	[54]		878 patches: 650 patches for training, 228 patches for test	US-Net, SSD from a post-processing sub-network	\
automatic segmentation	histopathological	2017	[53]		540 images: 110 images for training, 430 images for test	Convolution blocks are reduced; add a sub-convolution layer	\
segmentation	ventral nerve cord	2020	[57] 67		120 images	reducing the number of filters; adding a BN layer; adding Adam	IoU = 92.54%
segmentation	mitochondria and synapses	2018	[51]		\	2 distributed U-Nets	F1 = 72.3%
segmentation	retinal images	2018	[74]		28 retinal images: 70% for training, 30% for test	LabNet, two-stream U-Net share weights	SE = 79.78%, SP = 98.18%, ACC = 96.56%, AUC = 98.36%
segmentation	Colorectal polyps	2020	[54]		CVC-ColorectalDB dataset	DoubleU-Net, the information flows from the previous to the next decoding part	RE = 84.57%, PR = 95.92%
segmentation	adjacent cells	2020	[75]		cells dataset: 50 images, 80% for training, 10% for validation, 10% for test	DeepSplit: one encoder branch and two decoder branches	DSC = 91.1%, CDR = 93.3%
segmentation	human skin	2018	[74]		56 BC34 images: 46 for training, 10 for test	Munet: nested with three U-Nets	SE = 72.80%, SP = 95.26%, DICE = 78.86%, PR = 84.71%
segmentation	nucleus	2020	[73] 75		30 images: 16 images for training, 14 images for test	three U-Net branches; PDFR module is applied	AJ = 62.1%, DICE = 83.7%
segmentation	iris	2018	[74]		1000 images: 500 images for training, 500 images for test	ATT-U-Net: an attention mask is generated	Panoptic Quality = 68.1%
segmentation	retinal blood vessels	2020	[54]		40 fundus images: 20 images for training, 20 images for test	AA-U-Net: attention guided U-Net; atrous convolution	ACC = 96.56%, F1-score = 82.16%, JS = 95.68%, AUC = 98.67%
segmentation	retinal blood vessels	2019	[54]		STARF dataset	CS-Net: CAB and SAD is added	ACC = 97.62%, SE = 88.16%, SP = 98.40%, AUC = 99.02%
segmentation	retinal blood vessels	2019	[53]		20 fundus images: 50% for training, 50% for test	CSAU: attention gates is added	F1-score = 84.26%, SE = 84.60%, ACC = 96.72%
segmentation	retinal fundus	2020	[54]		50 for training, 51 for test	AG is added	For optic disc segmentation, an ACC of 99.67% and a DICE of 0.9817 are obtained. For optic cup segmentation, an ACC of 99.5% and a DICE of 0.9921 are obtained.
segmentation	cells	2020	[71]		135 images	AG is added	DICE of 0.89
segmentation	cell boundaries	2020	[54]		4000 images for training, 1000 images for validation, 500 images for test	AG is added; Residual blocks is added	SE = 97%, SP = 93%, F1-score = 95%, JS = 91%, DICE = 93%
segmentation	retinal blood vessel	2018	[51]		19,000 patches: 50% for training, 10% for validation	An identical structural deformation	\
segmentation	1 nerve	2018	[52] 90		30 images for training	Context-aware U-Net: placing a model on the connection	a mapping error = 0.000121, a read error = 0.0212, a pixel error = 0.0346
segmentation	retinal fundus vascular	2020	[53]		40 images, 20 images for training, 20 images for test	dense block is added; FReLU is added	SP = 98.14%, SE = 78.72%, ACC = 95.59%, AUC = 97.83
segmentation	retinal vessels	2019	[54]		40,000 image patches	dense block is applied; convolutional blocks is reduced; Residual idea is applied	SE = 79.86%, SP = 97.36%, ACC = 95.11%, AUC = 97.4%
segmentation	colorectal histopathology	2021	[54]		600 tissue images, 70% for training, 10% for validation, 10% for test	dense blocks is applied; dilated convolution is applied	DICE = 92.86%, IoU = 86.65%
segmentation	biomedical images	2018	[52]		165 biomedical images, 85 images for training, 85 images for test	MDU-Net: a multi-scale densely idea. Cross Dense connections is applied; Up Dense connections is applied; Down Dense connections is applied	\
segmentation	fluovent	2018	[53] 104		502407 training patches	DCSU: cascaded U-Net and dense connections is applied	IoU = 97.75%
segmentation	nucleus	2018	[53]		670 images	enhances the original U-Net skip connection	IoU of 92.63%
segmentation	cell, nuclei	2019	[53]			a new skip connection is applied	nuclei IoU = 94%, DICE = 95.4%
segmentation	nuclei	2020	[57]		1300 sub-images: 80% for training set, 10% for validation, 10% for test	Inception-ResNet-V2 network is integrated into U-Net + +	ACC = 95.05%, PR = 55.81%, RE = 60.33%, DICE = 53.97%
segmentation	OCT vessels	2019	[54]		100 images: 150 images for training, 40 images for test	the first U-Net segment intensity image, the segmentation result is used to the second U-Net	ACC = 94.4% ± 0.2%
segmentation	pigments and lake	2020	[59]		80 images	delete some skip connections; changing the number of channels	RMSE = 45.2187, Standard deviation = 7.8371
segmentation	color fundus photographs	2018	[114]		DRIVE: 40 images	delete the fourth connection between encoder's 112-channel feature map	SE = 87%, SP = 60%
segmentation	millow spore	2020	[113] 114		835 images: 550 images for training, 285 images for test	delete the three skip connections; pyramidal pool module is applied	MeU = 91.47%

4 Modified U-Net Related to Residual Block and Residual Idea

4.1 Only Residual Block

A depth of the network affects the extraction of features, but, as the network becomes deeper, the problem of overfitting and training errors in the network increases significantly. A Residual block is proposed to reuse the features of the previous layer to train a deeper network [90]. In [112], an improved U-Net based on Residual blocks has introduced. It is used to segment the regions of human-induced pluripotent Retinal Pigment Epithelial stem cells (iRPE) under Bright-field microscopy. This improved U-Net is tested on 1032 absorbance images of IRPE cells from Age-related Macular Degeneration (AMD) patients. In the dataset, the training set is composed of 800 images and the verification set is composed of 232 images. The experiment shows that this method is superior to the prior art method and the proposed deformed U-Net obtains the experimental result of a DICE of 0.8366.

In [113], a variant of U-Net with 9 Residual layers is proposed. It is used for Small extracellular vesicles (sEVs) collected by TEM to achieve good detection and segmentation performance. The architecture of variant U-Net is shown in Fig. 16. 688 sEVs of Mouse fibroblasts (L-cells), mouse embryonic fibroblast (MEF), human embryonic kidney 293 (HEK-293) and the ovarian cancer cell are used as a dataset. Under the dataset, the proposed method obtains a JS of 0.88.

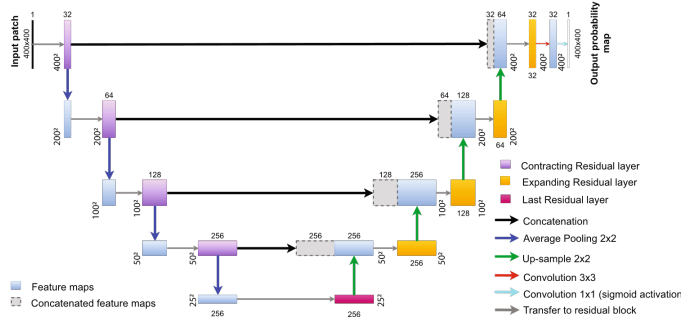


Fig. 16: The network architecture of variant of U-Net in [113] (Fig.2).

In [114], FusionNet with Residual block based on U-Net is proposed to automatically segment neuronal cells. The biggest difference between FusionNet and the original U-Net is that a Residual block containing 3 convolutions is added to each block. Like [112,113], 3 variable U-Nets proposed in the three papers are all based on U-Net and add Residual blocks. Unlike [112,113,113,113] transformed the original convolution block into a Residual block, FusionNet retains the original convolution block and inserts Residual blocks with three

convolutional. FusionNet is trained on 30 sections of *Drosophila* Electron Microscopic images (from [115]) and tested on a private dataset.

In [116], a simple concept network named Y-Net is used to segment different tissues in breast biopsy images to generate segmentation masks to assist breast cancer diagnosis. Y-Net differs from the baseline U-Net in that: Pyramid spatial pooling (PSP) and Residual convolutional blocks (RCB) are integrated into Y-Net, Y-Net adds two new hyperparameters and new fully connected layers.

The breast biopsy dataset containing 58 regions of interest (ROIs) is divided into a training set containing 29 images and a test set containing 29 images. Y-Net obtains a mIoU of 44.19% experimental results.

However, a large number of manual annotations are time-consuming and labor-intensive, a Multi-Tasking U-Net is proposed to solve this problem [117]. The Multi-Tasking U-Net is trained by coarse data labels to combine with a few pixel-wise annotations images. A Residual Multi-Tasking Block is proposed, each Multi-Tasking Block has three paths. The Multi-Tasking Block is composed of several sub-blocks with three tasks: task one is detection, task two is separation and task three is segmentation. Like [73], the Multi-Tasking U-Net is also a Multi-Tasking network. Unlike [73], the multi-tasking process of Multi-Tasking U-Net is embodied in a module instead of a decoder and Multi-Tasking U-Net has 1 more detection task. A training dataset contains 20 ice-cream Scanning Electron Microscopy (ESM) images and a test dataset contains 12 ice-cream SEM images. This Multi-Tasking U-Net obtains a DICE of 0.94 experimental results.

4.2 Residual Block & Skip Connection

In [118], in order to solve a problem that the classical U-Net does not perform well in the segmentation of some challenging datasets, MultiResUNet is proposed. Compared with the classical U-Net, the improved performance of MultiResUNet lies in the following two points. First, the MultiRes block is proposed and replaces all 2D convolution blocks in the classical U-Net. Second, a Res path with four 3×3 convolution and four short connections of Residual properties are creatively proposed to replace skip connections. MultiResUNet is tested and evaluated on five datasets, one of them obtains a JI of 91.65% experimental results (the dataset containing 97 fluorescence microscopy images from [119]). This architecture of MultiResUNet mentioned is shown in Fig. 17.

In [120], to minimize the limitations of the classical U-Net in some aspects and obtain more accurate segmentation results, DC-UNet is proposed. Like [118], the network structure of both uses the same Res path instead of skip connection. Unlike [118], DC-UNet creates a Dual-Channel block (consisting of six 3×3 Residual convolutions in two rows) to replace all convolution blocks of the original U-Net. The dataset from the ISBI 2012 challenge (a training set of 30 images and a test set of 30 images) is used to evaluate DC-UNet. An

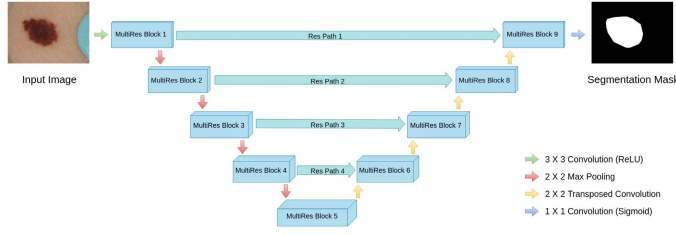


Fig. 17: The network architecture of MultiResUNet in [118] (Fig.5).

experiment is carried out 5-fold cross-validation and the experimental result of an average ACC of 92.62% is obtained.

In [121], in order to segment biomedical images quickly, effectively and with high PR, SD-UNet is proposed. It has three advantages: small model size (23 times smaller than U-Net), fewer parameters (eight times less than U-Net) and fast computing time. Compared with U-Net, its change is that a SD-UNet block is designed and replaces the original convolution block. From International Symposium on Biomedical Imaging (ISBI) challenge dataset, 30 fruit fly images under ssTEM are used to test SD-UNet to obtain an IoU of 83.26% and a DICE of 97.84%.

In [122], a Convolutional Long Short Term Memory (C-LSTM) block is integrated into U-Net and LSTM U-Net is proposed. The limitation of time information is incorporated into LSTM U-Net. Like [121], a new module is designed to replace the original convolution module. Unlike [121], the C-LSTM blocks of LSTM U-Net only exist in the encoder part. The structure facilitates the segmentation of single touch cells and partially visible cells. Furthermore, similar to an application of the LSTM module is discussed in this paper [123], which an extended LSTM block is designed based on the LSTM module and a Res block is designed based on the baseline U-Net and Residual. The LSTM U-Net is tested by the fluorescent simulated dataset (Fluo-N2DH-SIM+) in the Cell Tracking Challenge and a quantitative result of 0.811 is obtained.

In [93], since U-Net still has room for improvement in the task of nuclear segmentation, Rotation-Equivariant U-Net (REU-Net) is proposed to be used for histopathological images of seven different organs. Like [118, 120, 121], the REU-Net adds Residual blocks and modifies long connection. Unlike [118, 120, 121], in REU-Net, a long connection is between the second encoder and the third encoder. The dataset contains of 30 pathological images curated by [124]. In the dataset, 4 images are used as the training set and 7 images are used for validation and testing set respectively. The proposed method obtains an experimental result of an aggregated JS of 0.6291, an F1-score of 0.8469 and a DICE of 0.7980.

4.3 Residual Block & Recurrent

Models such as CNN can not accurately simulate high-level dependencies between object boundary points. Furthermore, in order to prevent overfitting and reduce the computational time, Recurrent Active Contour Evolution Network (RACE-Net) is proposed to segment Optic disc (OD) and Optic Cup (OC) in fundus images [125]. Feedforward neural network (FFNN) architecture is added to RACE-Net to simulate every step of the curve evolution. A generalized the level set based deformable models (LDM) evolving is simulated by RACE-net. RACE-Net utilizes the DRISHTI-GS1 dataset from [89], which contains 101 images in total (50 for training and 51 for testing). This RACE-Net-based method has the following experimental results. For OD segmentation, a DICE of 0.97 and a Boundary Localization Error (BLE) of 6.06 are obtained. For OC segmentation, a DICE of 0.87 and a BLE of 7.63 are obtained.

In [126, 127], Recurrent U-Net (RU-Net) and Recurrent Residual U-Net (R2U-Net) are developed to accurately segment the blood vessel images on the retina and skin cancer images. The biggest difference between RU-Net, R2U-Net and the baseline U-Net [27] is that the convolution units are different. RU-Net uses recurrent convolutional layers (RCL) and R2U-Net uses recurrent Residual convolutional layers (RRCL). Different variants of convolutional and recurrent convolutional units are shown in Fig. 18. The dataset contains 25000 patches of 20 images from Structured Analysis of the Retina (STARE) and CHASE_DB1 (of which 90% is train set and 10% is validation set) is used to train and verify RU-Net, R2U-Net. RU-Net obtains experimental results of an F1-score of 0.8396, a SE of 0.8108, an SP of 0.9871, an ACC of 97.06% and an AUC of 0.9909, respectively. R2U-Net obtains the experimental results of an F1-score of 0.8475, a SE of 0.8298, an SP of 0.9862, an ACC of 97.12% and an AUC of 0.9914, respectively.

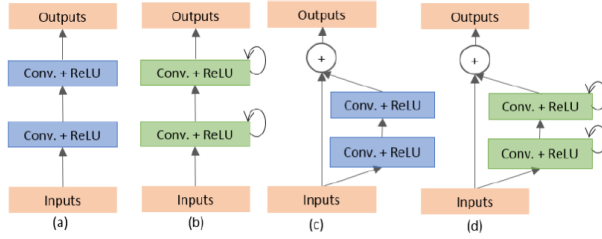


Fig. 18: Different variant of convolutional and recurrent convolutional units in [126] (Fig.4). (a) Forward convolutional units; (b) Recurrent convolutional block; (c) Residual convolutional unit; (d) Recurrent Residual convolutional units (RRCU).

In [128] (from the same team as [126]), R2U-Net is applied to the segmentation task of a nuclear cell. An unfolded version of the recurrent convolutional units is proposed. Like [126], R2U-Net from [128] has the same structure. Unlike [126], R2U-Net from [128] is applied to nuclear segmentation for the first time. This R2U-Net is evaluated on the Data Science Bowl Grand Challenge in 2018 (a total of 735 images, of which 536 are used for training, 134 are used for validation and 65 are used for testing). Finally, an experimental result shows that a DICE of 92.15% is obtained on the test set.

In [129], an R2U-Net model is developed to segment the nucleus. R2U-Net is introduced in [126], compared with R2U-Net from [126], this R2U-Net has not changed at all. A dataset used for image segmentation in experiments is composed of 735 cell images from the 2018 Data Science Bowl Grand Challenge. The database is divided into two groups: training and testing. The training dataset includes 650 images (in the training set, 80% is used for training and 20% is used for validation), while the testing dataset includes 65 images. Finally, this nuclei segmentation task obtains 92.15% testing ACC.

In [130], a baseline U-Net is introduced to segment label-free multiphoton microscopy (MPM) images of epithelial cells in prostate tissue. Segmentation results (segmented by the baseline U-Net) combined with the input of the baseline U-Net to obtain a merged image to train AlexNet [131] for classification. Nine tissue slides and 70 tissue microarray (TMA) cores of prostate cancer (PCa) tissues from 79 patients are used as a dataset. The dataset is curated by the First Affiliated Hospital of Fujian Medical University. Segmentation results are obtained: A mean F1-score of 0.839.

4.4 Inception-ResNet Block

Inception [132] and ResNet [90] receive widespread attention since they are creatively proposed. Different receptive fields are the characteristics of Inception structures and ResNet has a unique connection method to avoid vanishing gradients. In [132], Inception and ResNet are combined to form an Inception-ResNet block that combines the advantages of the above two structures.

In order to solve the problem of spatial information loss caused by continuous pooling and convolution in U-Net, a context encoder network (CE-Net) is proposed to segment medical images [133]. By combining Inception-ResNet-V2 block and atrous convolution, dense atrous convolution (DAC) blocks are proposed. The structural improvements are: (1) in the coding part, pre-trained ResNet-34 [90] replaces original ordinary blocks; (2) DAC blocks and Residual multi-kernel pooling (RMP) blocks are inserted into the context extractor section. This work utilizes an ORIGA dataset from [134], which contains 650 optic disc images in total. The proportions of the training set and test set are 50% and 50%, respectively. Under the dataset, CE-Net obtains an experimental result of an overlapping error of 0.058.

In order to solve the problem of vanishing gradient and excessive computation, in [135], a Dense-Inception U-net (DIU-Net) with an Inception-res block

is proposed to segment blood vessels. Like [133], Residual (short connection) and Inception are combined to form an Inception-Res block (The structure of the Inception-Res block is shown in Fig. 19). Unlike [133], the Dense-Inception block is applied in DIU-Net and the baseline Inception-Res block from [132] is replaced by a modified Residual Inception module. Similar to [80], three datasets (DRIVE [81], STARE [82] and CHASH_DB1 [83]) are used to evaluate the improved U-Net. The dataset has 136 samples of RGB images, of which 85% is used for training and 15% is used for testing. five-fold cross-validation is used in this experiment. Finally, a good experimental result is obtained (0.9582 DICE, 0.9338 JS, 0.9657 ACC, 0.7967 SE, 0.9863 SP, F0.8003 1-score and 0.9802 AUC).

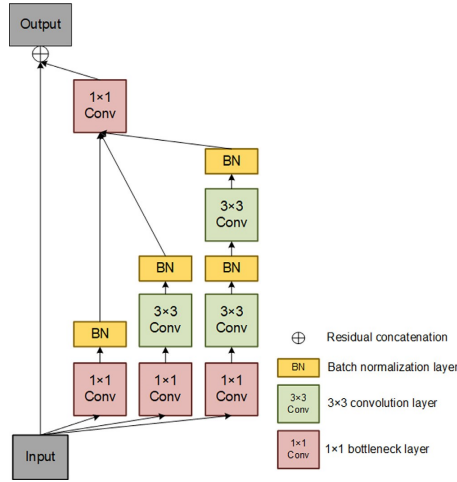


Fig. 19: The network architecture of Inception-Res block in [135] (Fig.2).

In order to better distinguish tiny features between different categories, in [136], a Mini-Inception-Residual-Dense network (MIRD-Net) is proposed to segment cervical cancer cells, blood vessels, and nuclei. Like [133, 135], MIRD-Net uses Inception blocks and Residual blocks. Unlike [133, 135], MIRD-Net integrates the Inception block, Residual block and dense block into a Mini-Inception-Residual-Dense Block, instead of being used independently for the network. A dataset of 30 images of nuclei from Data Science bowl 2018 is used. Under 5-fold cross-validation, an experimental result of a DICE of 0.954 is obtained.

In [137], an improved U-Net is proposed to automatically segment retinal vessel branches and bifurcations. In [137], the baseline convolution block from [27] is replaced by Residual Inception blocks from [132]. Different from [133, 135, 136], Firesqueeze blocks are inserted into U-Net. The improved U-Net is evaluated on a private dataset containing 65 Adaptive Optics Ophthalmoscopy (AOO) images of the eye fundus. In the dataset, 30 images are selected as the

training set, 5 images are selected as the validation set and 30 images are selected as the test set. Finally, experiments reveal that the improved U-Net obtains a PR of 0.97, a RE of 0.96 and an F1-score of 0.96.

4.5 Summary

According to the review above, we can see that, since 2018, modified U-Nets related to Residual block and Residual ideas are widely used. The variant U-Net without the Residual idea has some limitations, such as easy overfitting and slack training speed, while the Residual U-Net has better encode and decode information. The combination of Residual ideas and Inception, recurrent, skip connection changes can perform their respective advantages and the image segmentation efficiency is better. Table 3 summarizes the work done by different teams in using modified U-Net related to Residual block and Residual idea U-Net to analyze microscopic images.

Table 3: Summary of the modified U-Net related to Residual block and Residual idea U-Net for segmentation tasks. The second column “Detail” shows the application object.

Aim	Detail	Year	Reference	Team	Data Information	CNN type: points of improvement	Evaluation
segmentation	lymphatic cells	2019	[112]	G. Patel, et al.	800 images 212 for validation	Residual blocks instead of ordinary blocks	DICE = 83.66%
segmentation	aENs	2019	[113]	R. Gomez de Mariscal, et al.	688 images	9 Residual layers instead of ordinary blocks	J1 = 88%
segmentation	neutrophil cells	2018	[114]	T. M. Quen, et al.	30 for test	PastorNet: Residual block containing 3 convolutions is added to each block	Vrand = 97.4% Vrand = 98.99%
segmentation	tissues in breast biopsy	2018	[116]	S. Mohan, et al.	56 BICs 29 for training 29 for test	Y-Net: adds PSP and RCN; adds two new hyperparameters; adds a new fully connected layers	mIoU = 44.19%
segmentation	ice cream	2019	[117][120]	B. Ke, et al.	20 training 12 for test	Multi-Task U-Net: each Multi-Task Block has three paths	DICE = 0.94%
segmentation	fluorescence microscopy images	2020	[118]	N. Batschelet, et al.	97 fluorescence microscopy images	Residual block is added; Skip connection is changed	J1 = 91.633%
segmentation	cells	2021	[120]	A. Lou, et al.	ISBI-2012 challenge 30 for training 30 for test	Residual block is added; Skip connection is changed	ACC = 92.62%
segmentation	neutrophil cells	2020	[121]	P. K. Gudimov, et al.	ISBI challenge 30 fruit fly images	Residual block is added; Skip connection is changed	IoU = 83.28% DICE = 97.84%
segmentation	fluorescence microscopy images	2019	[122]	A. Archello, et al.	fluorescent simulated dataset Fluo-N2DM-SIM + 20 pathological images	Residual block is added; Skip connection is changed	Quantitative results = 81.1%
segmentation	nuclear	2019	[8][84]	B. Chidister, et al.	4 for training 7 for validation 7 images for test	Residual block is added; Skip connection is changed	AJ1 = 62.94% F1-score = 84.69% DICE = 79.86%
segmentation	OD and OC	2018	[123]	A. Chakraborty	301 images 50 for training, 51 for test	RACE-Net: Recurrent; FFNN architecture is added; LDM is added	DICE = 0.897% BLE = 7.63
segmentation	blood vessel	2019	[124], [127]	M. Z. Ahsan, et al.	25000 patches 90% for training, 10% for validation	RU-Net and R2U-Net (use RCL and RRCL)	F1-score = 84.75% SE = 82.98% SP = 98.62% ACC = 97.12% AUC = 99.14%
segmentation	nuclear cell	2018	[126]		735 images 536 for training, 124 for validation and 65 for test	R2U-Net	DICE = 92.15%
segmentation	nucleus	2018	[129]	A. M. Zahangir, et al.	650 images 40% for training, 20% for validation, 65 images for test	R2U-Net	ACC = 92.15%
segmentation	TMA cores of PCA tissues	2020	[130][133]	Q. Q. Yang, et al.	70 TMA cores	baseline U-Net	F1-score = 83.9%
segmentation	optic disc	2019	[133]	Z. W. Gu, et al.	650 images 50% for training 50% for test	CE-Net: Inception-BreNet-V2 block is applied; Atrous convolution is applied; Dense atrous convolution (DAC) blocks is applied	Overlapping error = 5.8%
segmentation	blood vessels	2020	[135]	Z. Zhang, et al.	136 RGB images 85% for training 15% for test	DIU-Net: Inception-eva block is applied; Dense-Inception block is applied	DICE = 92.82% JS = 93.38% ACC = 96.57% SE = 78.67% SP = 98.63% F1-score = 80.03% AUC = 98.02%
segmentation	cervical cancer cells	2020	[136]	Y. F. Huang, et al.	30 images	MHD-Net: Inception blocks and Residual blocks is applied; Mini-Inception-Residual-Dense block is applied	DICE = 95.4%
segmentation	retinal vessel branches and bifurcation	2020	[137][140]	I. Trimeche, et al.	30 for training five for validation 30 for test	Residual Inception blocks is applied; FusionNet blocks is applied	PR = 97% RE = 0.96% DSC = 96% F1-score of = 96%

5 Analysis of Methodology

5.1 Analysis of Several Typical Improvement Methods for U-Net

According to the survey of improved U-Net: Residual, attention and Inception are used more frequently in the improvement of U-Net. Because different datasets are used, each method cannot be compared longitudinally, so this paper analyzes from the perspective of the neural network itself.

The essence of Residual is a short connection, which means that it adds a skip connection that passes by the nonlinear transformation. A pre-made Resnet-34 in the feature encoder module is used to replace the convolutional layer and a maximum pooling layer. Some previous features can be reused, it solves the overfitting problem. Furthermore, because it adds a shortcut mechanism, it avoids the disappearance of the gradient and accelerates the network convergence. The papers involved in this article are [112–114, 116, 117].

Inception layers are a method of decomposing several convolutions from 1 convolution. The Inception layer connects convolutions of different filter sizes (1×1 , 3×3 , 5×5) and the mixing pool layer. Because of the difficulty in choosing the type of convolutional layer, Inception is proposed to automate the selection of various layers. The papers involved in this article are [133, 135–137]. In deep learning, Inception and Residual are two representative architectures. Inception uses different acceptance fields to expand the architecture. On the contrary, Residual uses a shortcut connection mechanism to avoid explosions and disappear gradients. Because of its existence, the neural network can have thousands of layers. In [132], the Inception-Resnet block combines the advantages of Inception and Residual to form a new module.

Attention is also an important way to improve U-Net, a bounding box of the potential region is regressed, an attention mask is generated and the attention mask is used as a weighted function. It merges discriminative feature maps into the model. Attention gates make the model pay more attention to vascular regions. The attention gate further improves the ACC on detailed vessels by additionally concatenating attention weights to features before output. The papers involved in this article are [78, 80, 84–88, 91, 92].

5.2 Analysis of the Outstanding Methods in Each Review Task

In the same dataset, some excellent improved U-Nets are proposed. For example, in the STARE dataset task, the best result is obtained by [84], where a CS-Net based on the self-attention mechanism is designed, so local features and their global dependencies can be effectively integrated. In addition, the spatial attention module is introduced, the context information is encoded into local features to increase representative capability.

For the Drishti-GS1 dataset segmentation task, the best result is obtained by multi-path recurrent U-Net with attention gate [86], which introduces the attention gating unit to obtain global information of the current input. In ad-

dition, maximum pooling and average pooling merge operations are introduced to the left and right branches respectively to reduce the error.

In the DRIVE dataset segmentation task, AA-UNet obtains the best segmentation results [80] which generates an attention mask and multiplies it with the feature map in the model. The main advantage of this model is that it can pay more attention to the blood vessel area. Furthermore, ordinary convolution is replaced by atrous convolution, which increases the receiving range and reduces the amount of calculation.

5.3 The Potential of the Mentioned Methods in this Survey in Other Research Fields

In addition, this review discussed the U-Net method not only can be applied to microscopic images, but also in other image analysis fields. Because of artifacts such as noise, weak edges and uneven intensity in Magnetic Resonance Imaging (MRI) images [138–143], many classic segmentation methods perform poorly. Deep learning neural networks based on U-Net can solve this problem.

However, there is no effective way to segment Computed Tomography (CT) images of gallstones. In [144], researchers proposed a new deep learning segmentation model based on U-Net with attentional upsampling blocks and spatial pyramid pools, which can give the importance of different shapes of target structures in the image. Therefore it is very suitable for segmentation of CT images [145–149].

Due to the existence of various ultrasound artifacts, accurate tumor segmentation is still a challenge. Therefore, a U-Net segmentation framework based on a deep learning structure is often used to segment ultrasound images. A following lists ultrasound image analysis [150–155].

No matter from the selection of datasets, image collection, preprocessing and from the design and proposal of an improved U-Net model, the deep artificial neural network summarized in this survey paper can provide support for research in other fields as well.

6 Conclusion and future work

In this survey paper, U-Net-based microscopic image analysis methods are comprehensively summarized. In addition, when summarizing the deep neural network method, the related work is grouped according to the type of improvement. In each type of improvement, performances with similar improvements idea has categorized similarly.

From classical review works in Sec. 2, U-Net without modification is used in cytology, microorganisms, nano-particles, histopathology. Deep learning techniques, especially deep convolutional neural networks, have achieved excellent results in the segmentation of microscopic images. Pathological images can help patients detect and treat diseases early. A sampling of contaminated water sources can separate the microorganisms in it, which is beneficial to protect

the environment. According to this review Sec. 2, the original U-Net is a very common method, but from the review works in Sec. 3 and Sec. 4, the deep learning method based on the improved U-Net is the most commonly used. This review works in Sec. 3 and Sec. 4, improved and novel network frameworks of U-Net tend to perform well under different datasets.

In the future, there is still room for improvement. First, researchers can combine various new microscopic images to develop new U-Net-based models to make them more suitable for new microscopic images, such as COVID-19. Secondly, there is no large-scale, full-label, open microscopic image dataset with many types and a very large dataset should be established to have a positive significance for the exploration of the field of microscopic image segmentation. Thirdly, for different medical image microscopy datasets, we should find an improved U-Net that is more suitable for them. Since a hospital processes a large amount of data every day, more accurate and faster output is also a goal with more potential and value in the future. Finally, only a few researchers study the improved U-Net composed of multiple U-Nets, which can better realize the flow of information. In the future, this improved U-Net composed of multiple U-Nets will be a more potential and valuable research direction, which is a key direction of our future work.

Acknowledgements

This work is supported by the “National Natural Science Foundation of China” (No. 61806047). We also thank Miss. Zixian Li and Mr. Guoxian Li for their important discussion in this work.

Declaration of Competing Interest

The authors declare that they have no conflict of interest in this paper.

References

1. Q. Wu, F. Merchant, and K. Castleman. *Microscope image processing*. Elsevier, 2010.
2. F. Zenhausern, M. Boyle, and H. Wickramasinghe. Apertureless near-field optical microscope. *Applied Physics Letters*, 65(13):1623–1625, 1994.
3. R. Toledo-Crow, P. Yang, Y. Chen, and M. Vaez-Iravani. Near-field differential scanning optical microscope with atomic force regulation. *Applied Physics Letters*, 60(24):2957–2959, 1992.
4. Y. Inouye and S. Kawata. Near-field scanning optical microscope with a metallic probe tip. *Optics Letters*, 19(3):159–161, 1994.
5. D. Williams and C. Carter. The transmission electron microscope. In *Transmission Electron Microscopy*, pages 3–17. 1996.
6. H. Seiler. Secondary electron emission in the scanning electron microscope. *Journal of Applied Physics*, 54(11):R1–R18, 1983.
7. J. Tersoff and D. Hamann. Theory of the scanning tunneling microscope. *Physical Review B*, 31(2):805, 1985.

8. G. Binnig, C. Quate, and C. Gerber. Atomic force microscope. *Physical Review Letters*, 56(9):930, 1986.
9. M. Duncan, J. Reintjes, and T. Manuccia. Scanning coherent anti-Stokes Raman microscope. *Optics Letters*, 7(8):350–352, 1982.
10. M. Adrian, J. Dubochet, J. Lepault, and A. McDowell. Cryo-electron microscopy of viruses. *Nature*, 308(5954):32–36, 1984.
11. C. Li, J. Zhang, F. Kulwa, S. Qi, and Z. Qi. A SARS-CoV-2 Microscopic Image Dataset with Ground Truth Images and Visual Features. In *Proc. of PRCV 2020*, pages 244–255, 2020.
12. C. Li, K. Wang, and N. Xu. A survey for the applications of content-based microscopic image analysis in microorganism classification domains. *Artificial Intelligence Review*, 51(4):577–646, 2019.
13. J. Zhang, C. Li, S. Kosov, M. Grzegorzczek, K. Shirahama, T. Jiang, C. Sun, Z. Li, and H. Li. LCU-Net: A novel low-cost U-Net for environmental microorganism image segmentation. *Pattern Recognition*, 115:107885, 2021.
14. X. Li, C. Li, M. Rahaman, X. Li, H. Sun, H. Zhang, Y. Zhang, X. Li, J. Wu, and Y. Yao. A Comprehensive Review of Computer-aided Whole-slide Image Analysis: from Datasets to Feature Extraction, Segmentation, Classification, and Detection Approaches. *Artificial Intelligence Review*, Online first:1–70, 2022.
15. X. Zhou and C. Li, M. Rahaman, Y. Yao, S. Ai, C. Sun, Q. Wang, Y. Zhang, M. Li, and X. Li. A comprehensive review for breast histopathology image analysis using classical and deep neural networks. *IEEE Access*, 8:90931–90956, 2020.
16. M. Rahaman, C. Li, X. Wu, Y. Yao, Z. Hu, T. Jiang, X. Li, and S. Qi. A survey for cervical cytopathology image analysis using deep learning. *IEEE Access*, 8:61687–61710, 2020.
17. S. Hore, S. Chakroborty, A. Ashour, N. Dey, A. Ashour, D. Sifaki-Pistolla, T. Bhattacharya, and S. Chaudhuri. Finding contours of hippocampus brain cell using microscopic image analysis. *Journal of Advanced Microscopy Research*, 10(2):93–103, 2015.
18. S. Øien, D. Wragg, H. Reinsch, S. Svelle, S. Bordiga, C. Lamberti, and K. Lillerud. Detailed structure analysis of atomic positions and defects in zirconium metal–organic frameworks. *Crystal Growth & Design*, 14(11):5370–5372, 2014.
19. W. Clelland and T. Fens. Automated rock characterization with SEM/image-analysis techniques. *SPE Formation Evaluation*, 6(04):437–443, 1991.
20. M. Pagliai and N. Vignozzi. Image analysis and microscopic techniques to characterize soil pore system. In *Physical Methods in agriculture*, pages 13–38. 2002.
21. A. Abell, K. Willis, and D. Lange. Mercury intrusion porosimetry and image analysis of cement-based materials. *Journal of Colloid and Interface science*, 211(1):39–44, 1999.
22. H. Nilsson. Remote sensing and image analysis in plant pathology. *Annual Review of Phytopathology*, 33(1):489–528, 1995.
23. N. Nilsson. *Principles of artificial intelligence*. Morgan Kaufmann, 2014.
24. D. Shen, G. Wu, and H. Suk. Deep learning in medical image analysis. *Annual Review of Biomedical Engineering*, 19:221–248, 2017.
25. G. Litjens, T. Kooi, B. Bejnordi, A. Setio, F. Ciompi, M. Ghafoorian, J. Laak, B. Ginneken, and C. Sánchez. A survey on deep learning in medical image analysis. *Medical Image Analysis*, 42:60–88, 2017.
26. N. Tajbakhsh, J. Shin, S. Gurudu, R. Hurst, C. Kendall, M. Gotway, and J. Liang. Convolutional neural networks for medical image analysis: Full training or fine tuning? *IEEE Transactions on Medical Imaging*, 35(5):1299–1312, 2016.
27. O. Ronneberger, P. Fischer, and T. Brox. U-net: Convolutional networks for biomedical image segmentation. In *Proc. of ICMICCA 2015*, pages 234–241, 2015.
28. J. Long, E. Shelhamer, and T. Darrell. Fully convolutional networks for semantic segmentation. In *Proc. of CVPR 2015*, pages 3431–3440, 2015.
29. S. Taghanaki, K. Abhishek, J. Cohen, J. Cohen-Adad, and G. Hamarneh. Deep semantic segmentation of natural and medical images: a review. *Artificial Intelligence Review*, pages 1–42, 2020.
30. G. Du, X. Cao, J. Liang, X. Chen, and Y. Zhan. Medical image segmentation based on u-net: A review. *Journal of Imaging Science and Technology*, 64(2):20508–1, 2020.

31. A. Colonna, F. Scarpa, and A. Ruggeri. Segmentation of corneal nerves using a u-net-based convolutional neural network. In *Computational Pathology and Ophthalmic Medical Image Analysis*, pages 185–192. 2018.
32. S. Seong and H. Park. Automated identification of neural cells in the multi-photon images using deep-neural networks. *arXiv: 1909.11269*, 2019.
33. M. Daniel, L. Atzrodt, F. Bucher, K. Wacker, S. Böhringer, T. Reinhard, and D. Böhringer. Automated segmentation of the corneal endothelium in a large set of ‘real-world’ specular microscopy images using the U-Net architecture. *Scientific Reports*, 9(1):1–7, 2019.
34. D. Núñez-Fernández, L. Ballan, G. Jiménez-Avalos, J. Coronel, and M. Zimic. Automatic semantic segmentation for prediction of tuberculosis using lens-free microscopy images. *arXiv: 2007.02482*, 2020.
35. A. Ojeda-Pat, A. Martin-Gonzalez, and R. Soberanis-Mukul. Convolutional Neural Network U-Net for Trypanosoma cruzi Segmentation. In *Proc. of ISICS 2020*, pages 118–131, 2020.
36. Z. Chen, X. Liu, J. Yang, E. Little, and Y. Zhou. Deep learning-based method for SEM image segmentation in mineral characterization, an example from Duvernay Shale samples in Western Canada Sedimentary Basin. *Computers & Geosciences*, 138:104450, 2020.
37. A. Oktay and A. Gurses. Automatic detection, localization and segmentation of nanoparticles with deep learning in microscopy images. *Micron*, 120:113–119, 2019.
38. S. Farley, J. Hodgkinson, O. Gordon, J. Turner, A. Soltoggio, P. Moriarty, and E. Hunsicker. Improving the segmentation of scanning probe microscope images using convolutional neural networks. *Machine Learning: Science and Technology*, 2(1):015015, 2020.
39. J. Jaworek-Korjakowska. A deep learning approach to vascular structure segmentation in dermoscopy colour images. *BioMed Research International*, 2018, 2018.
40. M. Meyer, P. Costa, A. Galdran, A. Mendonça, and A. Campilho. A deep neural network for vessel segmentation of scanning laser ophthalmoscopy images. In *Proc. of ICIAR 2017*, pages 507–515, 2017.
41. R. Webb, G. Hughes, and O. Pomerantzeff. Flying spot TV ophthalmoscope. *Applied Optics*, 19(17):2991–2997, 1980.
42. J. Zhang, B. Dashtbozorg, E. Bekkers, J. Pluim, R. Duits, and B. Romeny. Robust retinal vessel segmentation via locally adaptive derivative frames in orientation scores. *IEEE Transactions on Medical Imaging*, 35(12):2631–2644, 2016.
43. Z. Swiderska-Chadaj, T. Markiewicz, J. Gallego, G. Bueno, B. Grala, and M. Lorent. Deep learning for damaged tissue detection and segmentation in Ki-67 brain tumor specimens based on the U-net model. *Bulletin of the Polish Academy of Sciences. Technical Sciences*, 66(6), 2018.
44. Özgün Çiçek, A. Abdulkadir, S. Lienkamp, T. Brox, and O. Ronneberger. 3D U-Net: learning dense volumetric segmentation from sparse annotation. In *Proc. of ICMICCAI 2016*, pages 424–432, 2016.
45. Z. Fang, W. Yue, X. Zhitao, G. Lei, W. Jun, L. Yanbei, and W. Wen. Nanoparticle segmentation based on U-Net convolutional neural network. *Laser & Optoelectronics Progress*, 56(6):061005, 2019.
46. C. Fu, S. Lee, D. Ho, S. Han, P. Salama, K. Dunn, and E. Delp. Three dimensional fluorescence microscopy image synthesis and segmentation. In *Proc. of CVPR 2018*, pages 2221–2229, 2018.
47. D. Eschweiler, T. Spina, R. Choudhury, E. Meyerowitz, A. Cunha, and J. Stegmaier. CNN-based preprocessing to optimize watershed-based cell segmentation in 3D confocal microscopy images. In *Proc. of ISBI 2019*, pages 223–227, 2019.
48. L. Willis, Y. Refahi, R. Wightman, B. Landrein, José Teles, K. Huang, E. Meyerowitz, and Henrik Jönsson. Cell size and growth regulation in the Arabidopsis thaliana apical stem cell niche. *Proceedings of the National Academy of Sciences*, 113(51):E8238–E8246, 2016.
49. R. Fernandez, P. Das, V. Mirabet, E. Moscardi, J. Traas, J. Verdeil, G. Malandain, and C. Godin. Imaging plant growth in 4D: robust tissue reconstruction and lineaging at cell resolution. *Nature Methods*, 7(7):547, 2010.

50. K. Mosaliganti, R. Noche, F. Xiong, I. Swinburne, and S. Megason. ACME: automated cell morphology extractor for comprehensive reconstruction of cell membranes. *PLoS Comput Biol*, 8(12):e1002780, 2012.
51. L. Heinrich, J. Funke, C. Pape, J. Nunez-Iglesias, and S. Saalfeld. Synaptic cleft segmentation in non-isotropic volume electron microscopy of the complete drosophila brain. In *Proc. of ICMICCAI 2018*, pages 317–325, 2018.
52. H. Wang, D. Zhang, Y. Song, S. Liu, Y. Wang, D. Feng, H. Peng, and W. Cai. Segmenting neuronal structure in 3D optical microscope images via knowledge distillation with teacher-student network. In *Proc. of ISBI 2019*, pages 228–231, 2019.
53. M. Zhang, X. Li, M. Xu, and Q. Li. Image segmentation and classification for sickle cell disease using deformable u-net. *arXiv: 1710.08149*, 2017.
54. M. Zhang, X. Li, X. Xu, and Q. Li. RBC semantic segmentation for sickle cell disease based on deformable U-Net. In *Proc. of ICMICCAI 2018*, pages 695–702, 2018.
55. X. Xu, D. Papageorgiou, S. Abidi, M. Dao, H. Zhao, and G. Karniadakis. A deep convolutional neural network for classification of red blood cells in sickle cell anemia. *PLoS Computational Biology*, 13(10):e1005746, 2017.
56. X. Qin, C. Wu, H. Chang, H. Lu, and X. Zhang. Match Feature U-Net: Dynamic Receptive Field Networks for Biomedical Image Segmentation. *Symmetry*, 12(8):1230, 2020.
57. R. Rad, P. Saeedi, J. Au, and J. Havelock. Blastomere cell counting and centroid localization in microscopic images of human embryo. In *Proc. of MMSP 2018*, pages 1–6, 2018.
58. R. Rad, P. Saeedi, J. Au, and J. Havelock. Trophoctoderm segmentation in human embryo images via inceptioned U-Net. *Medical Image Analysis*, 62:101612, 2020.
59. C. Szegedy, W. Liu, Y. Jia, P. Sermanet, S. Reed, D. Anguelov, D. Erhan, V. Vanhoucke, and A. Rabinovich. Going deeper with convolutions. In *Proc. of CVPR 2015*, pages 1–9, 2015.
60. P. Saeedi, D. Yee, J. Au, and J. Havelock. Automatic identification of human blastocyst components via texture. *IEEE Transactions on Biomedical Engineering*, 64(12):2968–2978, 2017.
61. D. Matuszewski and I. Sintorn. Minimal annotation training for segmentation of microscopy images. In *Proc. of ISBI 2018*, pages 387–390, 2018.
62. G. Kylberg, M. Uppström, K. HEDLUND, G. Borgefors, and I. SINTORN. Segmentation of virus particle candidates in transmission electron microscopy images. *Journal of Microscopy*, 245(2):140–147, 2012.
63. I. Mocan, R. Itu, A. Ciurte, R. Danescu, and R. Buiga. Automatic Detection of Tumor Cells in Microscopic Images of Unstained Blood using Convolutional Neural Networks. In *Proc. of ICCP 2018*, pages 319–324, 2018.
64. Z. Xu, F. Sobhani, C. Moro, and Q. Zhang. Us-net for robust and efficient nuclei instance segmentation. In *Proc. of ISBI 2019*, pages 44–47, 2019.
65. W. Li, X. Qian, and J. Ji. Noise-tolerant deep learning for histopathological image segmentation. In *Proc. of ICIP 2017*, pages 3075–3079, 2017.
66. A. Fabijańska. Segmentation of corneal endothelium images using a U-Net-based convolutional neural network. *Artificial Intelligence in Medicine*, 88:1–13, 2018.
67. C. Kumar, M. TN, and A. Narasimhadhan. Cell Segmentation by Modified U-Net Architecture for Biomedical Images. In *Proc. of CONECCT 2020*, pages 1–6, 2020.
68. R. Bermúdez-Chacón, P. Márquez-Neila, M. Salzmann, and P. Fua. A domain-adaptive two-stream U-Net for electron microscopy image segmentation. In *Proc. of ISBI 2018*, pages 400–404, 2018.
69. D. Jha, M. Riegler, D. Johansen, P. Halvorsen, and H. Johansen. Doubleu-net: A deep convolutional neural network for medical image segmentation. In *Proc. of CBMS 2020*, pages 558–564, 2020.
70. J. Zhuang. Laddernet: Multi-path networks based on u-net for medical image segmentation. *arXiv: 1810.07810*, 2018.
71. K. Simonyan and A. Zisserman. Very deep convolutional networks for large-scale image recognition. *arXiv: 1409.1556*, 2014.
72. J. Bernal, F. Sánchez, G. Fernández-Esparrach, D. Gil, C. Rodríguez, and F. Vilarino. WM-DOVA maps for accurate polyp highlighting in colonoscopy: Validation vs.

- saliency maps from physicians. *Computerized Medical Imaging and Graphics*, 43:99–111, 2015.
73. A. Torr, D. Basaran, J. Sero, J. Rittscher, and H. Sailem. DeepSplit: Segmentation of Microscopy Images Using Multi-Task Convolutional Networks. In *Annual Conference on Medical Image Understanding and Analysis*, pages 155–167, 2020.
 74. A. Bozkurt, K. Kose, C. Alessi-Fox, M. Gill, J. Dy, D. Brooks, and M. Rajadhyaksha. A multiresolution convolutional neural network with partial label training for annotating reflectance confocal microscopy images of skin. In *Proc. of ICMICCAI 2018*, pages 292–299, 2018.
 75. B. Zhao, X. Chen, Z. Li, Z. Yu, S. Yao, L. Yan, Y. Wang, Z. Liu, C. Liang, and C. Han. Triple U-net: Hematoxylin-aware nuclei segmentation with progressive dense feature aggregation. *Medical Image Analysis*, 65:101786, 2020.
 76. G. Huang, Z. Liu, L. Maaten, and K. Weinberger. Densely connected convolutional networks. In *Proc. of CVPR 2017*, pages 4700–4708, 2017.
 77. O. Oktay, J. Schlemper, L. Folgoc, M. Lee, M. Heinrich, K. Misawa, K. Mori, S. McDonagh, N. Hammerla, and B. Kainz. Attention u-net: Learning where to look for the pancreas. *arXiv: 1804.03999*, 2018.
 78. S. Lian, Z. Luo, Z. Zhong, X. Lin, S. Su, and S. Li. Attention guided U-Net for accurate iris segmentation. *Journal of Visual Communication and Image Representation*, 56:296–304, 2018.
 79. H. Proença, S. Filipe, R. Santos, J. Oliveira, and L. Alexandre. The UBIRIS. v2: A database of visible wavelength iris images captured on-the-move and at-a-distance. *IEEE Transactions on Pattern Analysis and Machine Intelligence*, 32(8):1529–1535, 2009.
 80. Y. Lv, H. Ma, J. Li, and S. Liu. Attention guided U-Net with atrous convolution for accurate retinal vessels segmentation. *IEEE Access*, 8:32826–32839, 2020.
 81. N. Bansal and M. Dutta. Retina vessels detection algorithm for biomedical symptoms diagnosis. *International Journal of Computer Applications*, 71(20), 2013.
 82. Y. Guo, Ü. Budak, L. Vespa, E. Khorasani, and A. Şengür. A retinal vessel detection approach using convolution neural network with reinforcement sample learning strategy. *Measurement*, 125:586–591, 2018.
 83. S. Thangaraj, V. Periyasamy, and R. Balaji. Retinal vessel segmentation using neural network. *IET Image Processing*, 12(5):669–678, 2018.
 84. L. Mou, Y. Zhao, L. Chen, J. Cheng, Z. Gu, H. Hao, H. Qi, Y. Zheng, A. Frangi, and J. Liu. CS-Net: channel and spatial attention network for curvilinear structure segmentation. In *Proc. of ICMICCAI 2019*, pages 721–730, 2019.
 85. R. Li, M. Li, J. Li, and Y. Zhou. Connection sensitive attention u-net for accurate retinal vessel segmentation. *arXiv 2019. arXiv: 1903.05558*.
 86. Y. Jiang, F. Wang, J. Gao, and S. Cao. Multi-path recurrent u-net segmentation of retinal fundus image. *Applied Sciences*, 10(11):3777, 2020.
 87. H. Zhang, H. Zhu, and X. Ling. Polar coordinate sampling-based segmentation of overlapping cervical cells using attention U-Net and random walk. *Neurocomputing*, 383:212–223, 2020.
 88. N. Zhu, C. Liu, Z. Singer, T. Danino, A. Laine, and J. Guo. Segmentation with Residual Attention U-Net and an Edge-Enhancement Approach Preserves Cell Shape Features. *arXiv: 2001.05548*, 2020.
 89. J. Sivaswamy, S. Krishnadas, A. Chakravarty, G. Joshi, and A. Tabish. A comprehensive retinal image dataset for the assessment of glaucoma from the optic nerve head analysis. *JSM Biomedical Imaging Data Papers*, 2(1):1004, 2015.
 90. K. He, X. Zhang, S. Ren, and J. Sun. Deep residual learning for image recognition. In *Proc. CVPR 2016*, pages 770–778, 2016.
 91. W. Xiancheng, L. Wei, M. Bingyi, J. He, Z. Jiang, W. Xu, Z. Ji, G. Hong, and S. Zhaomeng. Retina blood vessel segmentation using a U-net based Convolutional neural network. *Procedia Comput Sci*, pages 1–11, 2018.
 92. J. Leng, Y. Liu, T. Zhang, P. Quan, and Z. Cui. Context-aware u-net for biomedical image segmentation. In *Proc. of BIBM 2018*, pages 2535–2538, 2018.
 93. B. Chidester, T. Ton, M. Tran, J. Ma, and M. Do. Enhanced rotation-equivariant u-net for nuclear segmentation. In *Proc. of CVPRW 2019*, page Online, 2019.

94. S. Jégou, M. Drozdal, D. Vazquez, A. Romero, and Y. Bengio. The one hundred layers tiramisu: Fully convolutional densenets for semantic segmentation. In *Proc. of CVPR 2017*, pages 11–19, 2017.
95. Y. Cheng, M. Ma, L. Zhang, C. Jin, L. Ma, and Y. Zhou. Retinal blood vessel segmentation based on Densely Connected U-Net. *Math. Biosci. Eng.*, 17:3088–3108, 2020.
96. K. He, X. Zhang, S. Ren, and J. Sun. Delving deep into rectifiers: Surpassing human-level performance on imagenet classification. In *Proc. of ICCV 2015*, pages 1026–1034, 2015.
97. C. Owen, A. Rudnicka, R. Mullen, S. Barman, D. Monekosso, P. Whincup, J. Ng, and C. Paterson. Measuring retinal vessel tortuosity in 10-year-old children: validation of the computer-assisted image analysis of the retina (CAIAR) program. *Investigative Ophthalmology & Visual Science*, 50(5):2004–2010, 2009.
98. C. Wang, Z. Zhao, Q. Ren, Y. Xu, and Y. Yu. Dense U-net based on patch-based learning for retinal vessel segmentation. *Entropy*, 21(2):168, 2019.
99. P. Samanta, G. Raipuria, and N. Singhal. Context Aggregation Network For Semantic Labeling In Histopathology Images. In *Proc. of ISBI 2021*, pages 673–676, 2021.
100. J. Li, S. Yang, X. Huang, Q. Da, X. Yang, Z. Hu, Q. Duan, C. Wang, and H. Li. Signet ring cell detection with a semi-supervised learning framework. In *Proc. of ICIPMI 2019*, pages 842–854, 2019.
101. K. Sirinukunwattana, J. Pluim, H. Chen, X. Qi, P. Heng, Y. Guo, L. Wang, B. Matuszewski, E. Bruni, and U. Sanchez. Gland segmentation in colon histology images: The glas challenge contest. *Medical Image Analysis*, 35:489–502, 2017.
102. J. Zhang, Y. Jin, J. Xu, X. Xu, and Y. Zhang. Mdu-net: Multi-scale densely connected u-net for biomedical image segmentation. *arXiv: 1812.00352*, 2018.
103. Y. Liu, W. Treible, A. Kolagunda, A. Nedo, P. Saponaro, J. Caplan, and C. Kambhamettu. Densely connected stacked u-network for filament segmentation in microscopy images. In *Proc. of ECCV 2018*, page Online, 2018.
104. C. Wu, Y. Xie, L. Shao, J. Yang, D. Ai, H. Song, Y. Wang, and Y. Huang. Automatic boundary segmentation of vascular Doppler optical coherence tomography images based on cascaded U-net architecture. *OSA Continuum*, 2(3):677–689, 2019.
105. Z. Zhou, M. RSiddiquee, N. Tajbakhsh, and J. Liang. Unet++: A nested u-net architecture for medical image segmentation. In *Deep Learning in Medical Image Analysis and Multimodal Learning for Clinical Decision Support*, pages 3–11. 2018.
106. Z. Zhou, M. Siddiquee, N. Tajbakhsh, and J. Liang. Unet++: Redesigning skip connections to exploit multiscale features in image segmentation. *IEEE Transactions on Medical Imaging*, 39(6):1856–1867, 2019.
107. H. Wang, Y. Li, and Z. Luo. An Improved Breast Cancer Nuclei Segmentation Method Based on UNet++. In *Proc. of ICCAI 2020*, pages 193–197, 2020.
108. A. Janowczyk and A. Madabhushi. Deep learning for digital pathology image analysis: A comprehensive tutorial with selected use cases. *Journal of Pathology Informatics*, 7, 2016.
109. M. Tsunomura, M. Shishikura, T. Ishii, R. Takahashi, and N. Tsumura. Segmentation of Microscopic Image of Colorants Using U-Net Based Deep Convolutional Networks for Material Appearance Design. In *International Conference on Image and Signal Processing*, pages 197–204, 2020.
110. X. Xu, T. Tan, and F. Xu. An improved U-net architecture for simultaneous arteriole and venule segmentation in fundus image. In *Proc. of ACMIUA 2018*, pages 333–340, 2018.
111. X. Liang and B. Wang. Wheat Powdery Mildew Spore Images Segmentation Based on U-Net. In *Journal of Physics: Conference Series*, volume 1631, page 012074, 2020.
112. G. Patel, H. Tekchandani, and S. Verma. Cellular segmentation of bright-field absorbance images using residual u-net. In *Proc. of ICAC 2019*, pages 1–5, 2019.
113. E. Gómez de Mariscal, M. Maška, A. Kotrbová, V. Pospíchalová, P. Matula, and A. Muñoz-Barrutia. Deep-learning-based segmentation of small extracellular vesicles in transmission electron microscopy images. *Scientific Reports*, 9(1):1–10, 2019.
114. T. Quan, D. Hildebrand, and W. Jeong. Fusionnet: A deep fully residual convolutional neural network for image segmentation in connectomics. *arXiv: 1612.05360*, 2016.

115. I. Arganda-Carreras, S. Turaga, D. Berger, D. Cireşan, A. Giusti, L. Gambardella, J. Schmidhuber, D. Laptev, S. Dwivedi, and J. Buhmann. Crowdsourcing the creation of image segmentation algorithms for connectomics. *Frontiers in Neuroanatomy*, 9:142, 2015.
116. S. Mehta, E. Mercan, J. Bartlett, D. Weaver, J. G. Elmore, and L. Shapiro. Y-Net: joint segmentation and classification for diagnosis of breast biopsy images. In *Proc. of ICMICCAI 2018*, pages 893–901, 2018.
117. R. Ke, A. Bugeau, N. Papadakis, P. Schuetz, and C. Schönlieb. A multi-task U-net for segmentation with lazy labels. *arXiv preprint arXiv:1906.12177*, 2019.
118. N. Ibtehaz and M. Rahman. MultiResUNet: Rethinking the U-Net architecture for multimodal biomedical image segmentation. *Neural Networks*, 121:74–87, 2020.
119. L. P. Coelho, A. Shariff, and R. F. Murphy. Nuclear segmentation in microscope cell images: a hand-segmented dataset and comparison of algorithms. In *Proc. of ISBI 2009*, pages 518–521, 2009.
120. A. Lou, S. Guan, and M. Loew. DC-UNet: rethinking the U-Net architecture with dual channel efficient CNN for medical image segmentation. In *Medical Imaging 2021: Image Processing*, volume 11596, page 115962T, 2021.
121. P. Gadosey, Y. Li, E. Adjei, T. Zhang, Z. Liu, P. Yamak, and F. Essaf. Sd-unet: Stripping down u-net for segmentation of biomedical images on platforms with low computational budgets. *Diagnostics*, 10(2):110, 2020.
122. A. Arbelle and T. Raviv. Microscopy cell segmentation via convolutional LSTM networks. In *Proc. of ISBI 2019*, pages 1008–1012, 2019.
123. H. Abdallah, B. Formosa, A. Liyanaarachchi, M. Saigh, S. Silvers, S. Arslanturk, D. Taatjes, L. Larsson, B. Jena, and D. Gatti. Res-CR-Net, a residual network with a novel architecture optimized for the semantic segmentation of microscopy images. *Machine Learning: Science and Technology*, 1(4):045004, 2020.
124. N. Kumar, R. Verma, S. Sharma, S. Bhargava, A. Vahadane, and A. Sethi. A dataset and a technique for generalized nuclear segmentation for computational pathology. *IEEE Transactions on Medical Imaging*, 36(7):1550–1560, 2017.
125. A. Chakravarty and J. Sivaswamy. RACE-net: a recurrent neural network for biomedical image segmentation. *IEEE Journal of Biomedical and Health Informatics*, 23(3):1151–1162, 2018.
126. M. Alom, M. Hasan, C. Yakopcic, T. Taha, and V. Asari. Recurrent residual convolutional neural network based on u-net (r2u-net) for medical image segmentation. *arXiv: 1802.06955*, 2018.
127. M. Alom, C. Yakopcic, M. Hasan, T. Taha, and V. Asari. Recurrent residual U-Net for medical image segmentation. *Journal of Medical Imaging*, 6(1):014006, 2019.
128. M. Alom, C. Yakopcic, T. Taha, and V. Asari. Nuclei segmentation with recurrent residual convolutional neural networks based U-Net (R2U-Net). In *Proc. of NAECON 2018*, pages 228–233, 2018.
129. A. Zahangir, C. Yakopcic, T. Taha, and V. Asari. Microscopic Nuclei Classification, Segmentation and Detection with improved Deep Convolutional Neural Network (DCNN) Approaches. *arXiv e-prints*, pages arXiv–1811, 2018.
130. Q. Yang, Z. Xu, C. Liao, J. Cai, Y. Huang, H. Chen, X. Tao, Z. Huang, J. Chen, and J. Dong. Epithelium segmentation and automated Gleason grading of prostate cancer via deep learning in label-free multiphoton microscopic images. *Journal of Biophotonics*, 13(2):e201900203, 2020.
131. A. Krizhevsky, I. Sutskever, and G. Hinton. Imagenet classification with deep convolutional neural networks. *Advances in Neural Information Processing Systems*, 25:1097–1105, 2012.
132. C. Szegedy, S. Ioffe, V. Vanhoucke, and A. Alemi. Inception-v4, inception-resnet and the impact of residual connections on learning. In *Proc. of AAAI 2017*, volume 31, 2017.
133. Z. Gu, J. Cheng, H. Fu, K. Zhou, H. Hao, Y. Zhao, T. Zhang, S. Gao, and J. Liu. Cenet: Context encoder network for 2d medical image segmentation. *IEEE Transactions on Medical Imaging*, 38(10):2281–2292, 2019.
134. Z. Zhang, F. Yin, J. Liu, W. Wong, N. Tan, B. Lee, J. Cheng, and T. Wong. Origa-light: An online retinal fundus image database for glaucoma analysis and research. In *Proc. of AICEMB 2010*, pages 3065–3068, 2010.

135. Z. Zhang, C. Wu, S. Coleman, and D. Kerr. DENSE-INception U-net for medical image segmentation. *Computer Methods and Programs in Biomedicine*, 192:105395, 2020.
136. Y. Huang, X. Li, C. Yan, L. Liu, and H. Dai. MIRD-Net for Medical Image Segmentation. In *Pacific-Asia Conference on Knowledge Discovery and Data Mining*, pages 207–219, 2020.
137. I. Trimeche, F. Rossant, I. Bloch, and M. Pâques. Fully automatic CNN-based segmentation of retinal bifurcations in 2D adaptive optics ophthalmoscopy images. In *Proc. of IPTA 2020*, pages 1–6, 2020.
138. G. Piantadosi, M. Sansone, and C. Sansone. Breast segmentation in mri via u-net deep convolutional neural networks. In *Proc. of ICPR 2018*, pages 3917–3922, 2018.
139. F. Wang, R. Jiang, L. Zheng, C. Meng, and B. Biswal. 3d u-net based brain tumor segmentation and survival days prediction. In *Proc. of MICCAI-BW 2019*, pages 131–141, 2019.
140. B. Lee, N. Yamanakkanavar, and J. Choi. Automatic segmentation of brain MRI using a novel patch-wise U-net deep architecture. *Plos One*, 15(8):e0236493, 2020.
141. L. Rundo, C. Han, Y. Nagano, J. Zhang, R. Hataya, C. Militello, A. Tangherloni, M. Nobile, C. Ferretti, and D. Besozzi. USE-Net: Incorporating Squeeze-and-Excitation blocks into U-Net for prostate zonal segmentation of multi-institutional MRI datasets. *Neurocomputing*, 365:31–43, 2019.
142. A. Kermi, I. Mahmoudi, and M. Khadir. Deep convolutional neural networks using U-Net for automatic brain tumor segmentation in multimodal MRI volumes. In *Proc. of MICCAI-BW 2018*, pages 37–48, 2018.
143. Y. Chen, Z. Cao, C. Cao, J. Yang, and J. Zhang. A modified U-Net for brain Mr image segmentation. In *Proc. of ICCCS 2018*, pages 233–242, 2018.
144. T. Song, F. Meng, A. Rodriguez-Paton, P. Li, P. Zheng, and X. Wang. U-next: a novel convolution neural network with an aggregation u-net architecture for gallstone segmentation in CT images. *IEEE Access*, 7:166823–166832, 2019.
145. H. Roth, H. Oda, X. Zhou, N. Shimizu, Y. Yang, Y. Hayashi, M. Oda, M. Fujiwara, K. Misawa, and K. Mori. An application of cascaded 3D fully convolutional networks for medical image segmentation. *Computerized Medical Imaging and Graphics*, 66:90–99, 2018.
146. H. Roth, C. Shen, H. Oda, M. Oda, Y. Hayashi, K. Misawa, and K. Mori. Deep learning and its application to medical image segmentation. *Medical Imaging Technology*, 36(2):63–71, 2018.
147. Y. Chen, Y. Lin, C. Wang, C. Lee, W. Lee, T. Wang, and C. Chen. Coronary artery segmentation in cardiac CT angiography using 3D multi-channel U-net. *arXiv: 1907.12246*, 2019.
148. N. Saeedizadeh, S. Minaee, R. Kafieh, S. Yazdani, and M. Sonka. COVID TV-Unet: Segmenting COVID-19 chest CT images using connectivity imposed Unet. *Computer Methods and Programs in Biomedicine Update*, 1:100007, 2021.
149. Y. Weng, T. Zhou, Y. Li, and X. Qiu. Nas-unet: Neural architecture search for medical image segmentation. *IEEE Access*, 7:44247–44257, 2019.
150. R. Almajalid, J. Shan, Y. Du, and M. Zhang. Development of a deep-learning-based method for breast ultrasound image segmentation. In *Proc. of ICMLA 2018*, pages 1103–1108, 2018.
151. Y. Wang, C. Wei, Z. Wang, Q. Lu, and C. Wang. A more streamlined u-net for nerve segmentation in ultrasound images. In *Proc. of CAC 2018*, pages 101–104, 2018.
152. X. Li, Y. Hong, D. Kong, and X. Zhang. Automatic segmentation of levator hiatus from ultrasound images using U-net with dense connections. *Physics in Medicine & Biology*, 64(7):075015, 2019.
153. J. Yang, M. Faraji, and A. Basu. Robust segmentation of arterial walls in intravascular ultrasound images using Dual Path U-Net. *Ultrasonics*, 96:24–33, 2019.
154. M. Amiri, R. Brooks, B. Behboodi, and H. Rivaz. Two-stage ultrasound image segmentation using U-Net and test time augmentation. *International Journal of Computer Assisted Radiology and Surgery*, 15(6):981–988, 2020.
155. M. Amiri, R. Brooks, and H. Rivaz. Fine tuning u-net for ultrasound image segmentation: Which layers? In *Domain Adaptation and Representation Transfer and Medical Image Learning with Less Labels and Imperfect Data*, pages 235–242. 2019.